Quantifying Greenhouse Gas Methane Emissions from Simulated Plumes: A Hybrid Computational Fluid Dynamics (CFD) and Image-Based Approach

by

Ghazal Mansoori
B.Sc., Shiraz University, 2019

A Thesis Submitted in Partial Fulfillment of the
Requirements for the Degree of

MASTERS OF APPLIED SCIENCE

in the Department of Electrical and Computer Engineering

University of Victoria

We acknowledge and respect the Lək̓ʷəŋən (Songhees and X̓ʷsepsəm/Esquimalt) Peoples on whose territory the university stands, and the Lək̓ʷəŋən and W̱SÁNEĆ Peoples whose historical relationships with the land continue to this day.

Quantifying Greenhouse Gas Methane Emissions from Simulated Plumes: A Hybrid Computational Fluid Dynamics (CFD) and Image-Based Approach

by

Ghazal Mansoori
B.Sc., Shiraz University, 2019

Supervisory Committee

Dr. Thomas E. Darcie, Supervisor
(Department of Electrical and Computer Engineering)

Dr.Robert Levi Smith, Supervisor
(Department of Electrical and Computer Engineering)

Supervisory Committee

Dr. Thomas E. Darcie, Supervisor
(Department of Electrical and Computer Engineering)

Dr.Robert Levi Smith, Supervisor
(Department of Electrical and Computer Engineering)

ABSTRACT

Given methane's role as a potent greenhouse gas with a significantly higher short-term global warming potential than carbon dioxide, its accurate quantification is critical for early detection and mitigation. This thesis presents a simulation-driven framework for quantifying greenhouse gas methane leak rates using image-based projections derived from computational fluid dynamics (CFD). Methane emissions with field-representative leak rates were modeled in open-air environments using three-dimensional (3D) simulations under varying wind and leak source conditions. The resulting volumetric data were transformed to mimic the output of remote optical sensing systems, enabling leak rate estimation via a MATLAB-based algorithm grounded in the principles of mass conservation. This approach offers a practical foundation for remote methane quantification, with potential applications in sensor validation, environmental monitoring, and climate action strategies focused on emission reductions.

Contents

List of Tables

List of Figures

List of Acronyms

2D two-dimensional. ix, 3, 43, 48–54, 57, 59, 60, 63, 70, 71, 79

3D three-dimensional. iii, vi, ix, 3, 21, 34, 36, 42–44, 48, 49, 52, 53, 55, 63, 65, 66, 70, 79

CFD Computational Fluid Dynamics. v–vii, ix, x, 3–5, 21, 30, 31, 48, 49, 51, 52, 54, 59, 61, 63, 65, 70–77, 79–81

CV control volume. 23

CW continuous wave. 15

DAS Direct Absorption Spectroscopy. viii, 9–12, 15, 20

EPA Environmental Protection Agency. 2

FEM Finite Element Method. 31

FMCW Frequency Modulation Continuous Wave. 9, 15, 17–20, 52

FVM Finite Volume Method. 31

GWP global warming potential. 1

HITRAN High-resolution Transmission. 7

IAP Integrated Absorption Path. 8, 9

IR infrared. 6, 7, 9, 12

LES Large Eddy Simulation. 63

Lidar light detection and ranging. 15–18, 20

LO local oscillator. 16, 18

LPF low-pass filter. 14

Ma Mach number. 26

OGI Optical Gas Imaging. viii, 20, 21

RANS Reynolds-Averaged Navier-Stokes. 38, 40

Re Reynolds number. 25

RTT Reynolds Transport Theorem. 27

SNR signal-to-noise ratio. 19

TDS Transport of Diluted Species. 39–41

TF Turbulent Flow. 41

WMS Wavelength Modulation Spectroscopy. 9, 12–15, 18, 20, 52

ACKNOWLEDGEMENTS

I would like to thank the following for their support throughout my studies:

My supervisors, for their mentorship, encouragement, and patience, and for guiding me by breaking each goal into clear, achievable steps.

MITACS and NSERC, for supporting me with a scholarship.

My colleagues, for their encouragement and the thoughtful discussions that supported this journey.

My family, for their love and support in my low moments.

My husband, whose encouragement carried me through every challenge and every victory.

DEDICATION

Dedicated to those who learn, share, and inspire others, helping knowledge grow and pass on.

Chapter 1

Introduction

1.1 Methane: a Greenhouse Gas

Methane (CH_4) is a highly potent greenhouse gas with major implications for global warming and climate stability. Although its atmospheric concentration is much lower than that of carbon dioxide (CO_2), methane is considerably stronger at trapping heat. Over a 20-year time period, methane's global warming potential (GWP) is approximately 84 times greater than that of CO_2 (IPCC, 2021)[1]. This makes it one of the most impactful short-lived climate pollutants, with an atmospheric lifetime of around 12 years[2].

Since the pre-industrial era, atmospheric methane concentrations have increased by 161.9%, driven primarily by human activities such as fossil fuel extraction, agriculture, and waste management (EPA, 2024)[3]. In Canada, methane contributes approximately 13% to total greenhouse gas emissions, making it a critical target for reduction strategies [4]. However, recent studies show that national inventories may significantly underestimate actual methane emissions in Canada[5][6]. These findings reinforce the critical role this greenhouse gas plays in both national and global emission reduction and climate strategies, underscoring the need to detect, monitor, and quantify methane emissions accurately.

Because of its high GWP and short lifetime, reducing methane emissions is viewed as a key strategy for rapid climate benefits[1]. Recognizing this, international efforts, including the Global Methane Pledge, aim to reduce global methane emissions by at least 30% from 2020 levels by 2030[7]. These coordinated efforts underscore the necessity and urgency of methane mitigation as a critical part of the near-term climate strategy[8].

Reducing methane emissions requires not only the detection of the emission source but also timely intervention through repair or mitigation, as demonstrated in one study[9]. To support these actions, it is essential to identify the presence of methane and accurately quantify its release rate, while monitoring in real-time[10]. In many cases, methane enters the atmosphere unintentionally through leaks in infrastructure. These leaks often go unnoticed, which underscores the need for timely detection and quantification.

To standardize methane leak assessments, regulatory bodies like the Environmental Protection Agency (EPA) express emission rates in grams per hour (g/h)[11] . This metric, often referred to as **leak rate**, provides a consistent way to evaluate emission severity and prioritize mitigation efforts. Throughout this thesis, methane quantification refers specifically to estimation of leak rates in grams per hour (g/h), following this regulatory standard.

Methane is an invisible and odorless gas that tends to rise and disperse quickly in the atmosphere due to buoyancy and wind-driven turbulence[12]. These characteristics make it difficult to locate the leak source and understand how the gas spreads under real-world conditions. While localized methane detection is achievable with well-established point-sensing technologies, the accurate estimation of leak rate and spatial distribution of methane concentration remains technically challenging[13]. This complexity arises from the inherently dynamic, three-dimensional (3D) behavior of gas dispersion in open environments, which evolves continuously with atmospheric conditions.

1.2 Motivation

As explained in Section 1.1, precise quantification and continuous monitoring of methane emissions are fundamental for effective mitigation strategies. Recent studies have also explored image-based approaches for detecting methane emissions. For instance, VideoGasNet [14] uses infrared video data to classify leak severity into discrete categories. However, its focus is on classification rather than continuous leak rate quantification. In contrast, the present work aims to estimate actual leak rates using a simulation-driven, image-based approach.

Although methane detection technologies, and to a lesser extent, quantification methods, have improved in recent years, several critical limitations remain. These include restricted spatial coverage and sensitivity thresholds that may miss smaller or intermittent leaks [15], as well as high variability due to changing environmental conditions and background noise [16] and logistical challenges in field deployment. Validating system performance under diverse real-world conditions also remains a persistent challenge [16]. These limitations motivate the development of complementary tools that offer controlled, repeatable testing environments to better understand methane leak behavior and support robust calibration and validation of detection and quantification technologies.

To address this need, numerical simulations have therefore emerged as a powerful method for investigating the physics of methane dispersion in realistic environments. The **first phase** of this work numerically models small-scale methane leaks using computational fluid dynamics (CFD) under simplified atmospheric scenarios. The 3D simulations capture both the near-source dynamics and downstream dispersion of methane, providing a reliable ground truth leak rate that is typically unknown in real-world scenarios. This enables systematic evaluation of how leak rate, wind condition, and source geometry influence plume behavior.

However, a key challenge arises when comparing simulation data with real optical gas sensing systems; simulations in this study produce full 3D concentration fields, while those systems capture only line-of-sight integrated absorption path of methane (IAP(x,y)). Converting such 2D optical data into quantitative leak rates remains a recognized challenge [17].

To bridge this gap, the **second phase** of this thesis develops an image-based post-processing framework. This workflow is illustrated in Figure 1.1. The 3D CFD simulations are then optically projected into synthetic IAP images that replicate what a gas detection or imaging system would capture from a methane plume. A MATLAB-based algorithm then processes the IAP image data to estimate the corresponding methane mass flow rate, combining the integrated concentration distribution with the wind field information. This framework enables direct comparison with real measurements and yields consistent leak rate quantification.

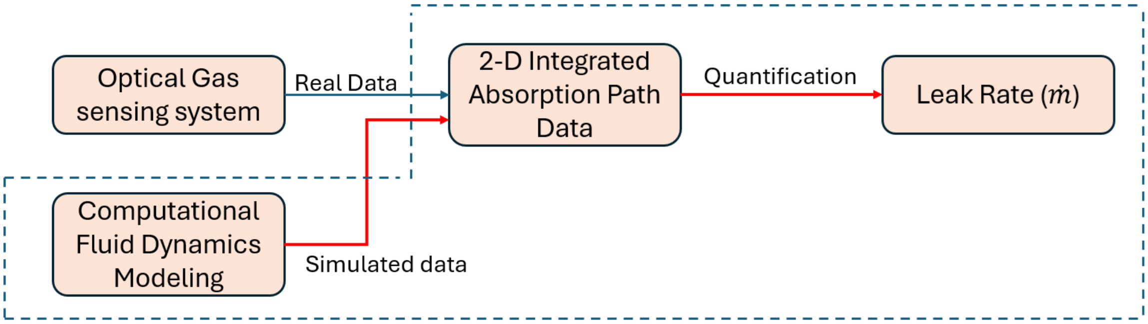

Figure 1.1: Simulation-informed methane leak quantification workflow. The dashed boxes indicate the two-phase framework developed in this study

In principle, methane leak rate can be calculated using the expression $\dot{m} = \rho\,\mathbf{V}\cdot\mathbf{A}$ (explained in Chapter 2), where ρ is the gas density, $\mathbf{V}$ is the local velocity vector at the leak source, and $\mathbf{A}$ is the cross-sectional area normal to the leak surface. In cases where the flow is normal to the leak opening, this simplifies to $\dot{m} = \rho\,V\,A$ where V denoting the magnitude of the normal velocity and A is the leak cross-sectional area. However, in remote sensing scenarios, neither the leak geometry nor the velocity at the leak point is typically known or accessible. This makes direct application of this equation impractical. As a result, there is a clear need for alternative methods that can infer leak rates based on remotely sensed measurements, such as gas concentration fields, rather than relying on direct measurement of leak parameters. This challenge forms the core motivation for the image-based quantification framework developed in this work.

This integrated, two-phase approach, combining high-resolution CFD modeling with an image-based quantification framework, aims to bridge the methodological gap between numerical simulation and remote sensing. By enabling simulated plumes to be interpreted in the same terms as real-world remote optical measurements, it supports the development, testing, and calibration of methane detection technologies. Ultimately, this work contributes to more accurate and scalable methane leak quantification, and strengthens the foundation for more responsive and effective mitigation strategies.

1.3 Agenda

The remainder of this thesis is structured as follows:

Chapter 2 provides the theoretical background relevant to this study. It covers methane detection principles, gas dispersion fundamentals, the operation of optical sensing methods used in emission detection, and numerical modeling.

Chapter 3 presents the CFD modeling approach developed to simulate methane dispersion into the atmosphere under various leak and atmospheric scenarios. It describes the model setup, physics interfaces, boundary conditions, and solver configuration.

Chapter 4 introduces an image-based framework developed in MATLAB. It details how volumetric simulation data are transformed into optical analogs through projection techniques and explains the leak-rate quantification algorithm defined in this study.

Chapter 5 contains the results and validation. It includes comparisons between simulation-based quantification and known ground-truth leak rates, evaluating the accuracy, and practical utility of the proposed approach.

Chapter 6 concludes the thesis with a summary of key findings, a critical discussion of the methodology, limitations, and suggestions for future research directions.

Chapter 2

Theoretical Background

2.1 Infrared Absorption Spectroscopy and the Beer-Lambert Law

Laser absorption spectroscopy has recently become a reliable method for gas analysis in the infrared (IR) spectrum [18, 19]. This technique enables both the identification of gas species and the quantitative measurement of their local concentrations [19]. This technique involves directing laser light through a gas plume, where gas molecules selectively absorb light at characteristic wavelengths that are unique to its molecular structure [20].

These absorption features occur when gas molecules absorb infrared light, causing rotational and vibrational excitations, or transitions of electrons between energy levels within the atoms of the gas molecules. This behavior forms the foundation of molecular spectroscopy [19] [17].

The interaction between light and gas is properly defined by the **Beer-Lambert Law**, which describes the relationship between light absorption and the gas of interest's concentration over a path length:

$$P_{out} = P_{in} \cdot e^{-\alpha C l} \tag{2.1}$$

where:

- P_{out} is the transmitted power,
- P_{in} is the incident beam power,

- α is the absorption coefficient,
- C is gas concentration,
- l is the optical path length

For gases such as methane, the absorption coefficient α is wavelength-dependent and can be expressed as [19] :

$$\alpha(\nu) = N_0 S(T)\phi(\nu, p, T) \tag{2.2}$$

Here, $S(T)$ is the line strength and $\phi(\nu, p, T)$ is the lineshape function, which describes how absorption is distributed around central frequency; these parameters are available from the High-resolution Transmission (HITRAN) molecular absorption database, which is an informative resource for spectral line parameters of atmospheric gases.

Understanding α is essential for selecting the laser wavelength in gas (i.e methane in this study) detection systems. Figure 2.1 presents the near-IR absorption spectrum of methane, generated from the HITRAN database [19], which is crucial to identify the specific wavelength at which methane absorbs light. The sharp dips correspond to specific absorption lines, which reflect the wavelength dependence of the absorption coefficient α. These lines are essential for both laser wavelength selection and for the application of the Beer–Lambert Law in optical detection systems.

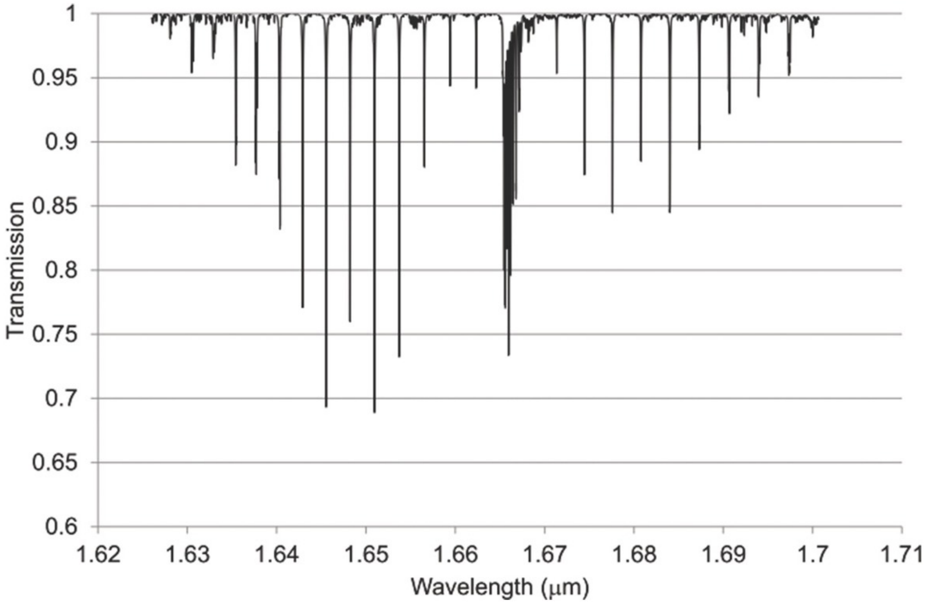

Figure 2.1: Near-infrared transmission spectrum of methane CH_4, generated using the HITRAN database.

In practical scenarios such as remote sensing, the gas concentration often varies spatially along the beam path. A key derived quantity in these systems is the Integrated Absorption Path (IAP), which represents the total amount of gas concentration over the optical path length [21] [13] [22], as follows:

$$IAP = \int_0^l C(x)dx \tag{2.3}$$

Here, $C(x)$ is the gas concentration at position x and l is the optical path length.

IAP captures the full absorption contribution from nonuniform gas distributions, making it a more realistic and applicable measure than uniform-concentration assumptions. This concept is especially useful in environmental sensing and leak quantification, where plume concentrations change continuously in space.

To connect this to measurable quantities, the Beer–Lambert Law can be adapted using IAP, resulting in:

$$\frac{P_{out}}{P_{in}} = e^{-\alpha \cdot IAP} \tag{2.4}$$

This version directly links measured transmission to integrated gas concentration, and is widely used in optical gas detection techniques[21][22]

Regarding methane monitoring, the Beer-Lambert Law enables accurate estimation of IAP by measuring light attenuation at methane's resonant wavelengths. Several strong absorption lines of methane exist in the near- and mid-infrared (e.g., around 1.65 μm, 2.3 μm, and 3.3 μm). This principle underpins a wide range of environmental sensing and ranging techniques, including Direct Absorption Spectroscopy (DAS), Wavelength Modulation Spectroscopy (WMS), and Frequency Modulation Continuous Wave (FMCW) methods which will be discussed in the following section.

In this thesis, the Beer-Lambert law provides the theoretical foundation to understand how light interacts with methane gas to extract concentration information from laser-based systems. It supports the generation of IAP maps, and enables improved ways to develop techniques for methane quantification, which is critical for environmental monitoring and effective analysis of gas leaks in remote sensing systems.

2.2 Laser-Based Optical Sensing Techniques

In IR absorption spectroscopy, as outlined in the Beer-Lambert Law section, a central objective is to measure light absorption across a known path length. In practical systems, this is often achieved by measuring the relative change in light intensity, typically expressed as the ratio of $\Delta P/P_{in}$ which corresponds to the total absorption by the gas.

This relationship can be described in an alternative form of Beer-Lambert Law as shown in equation 2.5 and approximated linearly when absorption is weak[19]. When combined with spectral lineshape analysis, this measurement is essential to derive important gas parameters, such as concentration, pressure, and temperature[19].

Several well-established methods exist to perform this measurement. Techniques such as DAS and WMS, are commonly used for gas detection. In specialized applications, FMCW techniques have been adapted for range-resolved gas sensing, combining concentration measurement with spatial localization [13]. The following sections describe these methods in more detail.

$$\frac{\Delta P}{P_{in}} = \frac{P_{in} - P_{out}}{P_{in}} = 1 - e^{-\alpha C l} \approx \alpha C l \qquad \text{for } \alpha C l \ll 1 \tag{2.5}$$

2.2.1 Direct Absorption Spectroscopy

In DAS, a laser beam, typically operated in continuous-wave mode but frequency-tuned (modulated) across the absorption line, passes through a gas cell of known volume. The technique directly measures the attenuation in light intensity between the incident and transmitted beams to determine the absorption ratio ($\Delta P/P_{in}$) and thus provides data to estimate gas parameters.

Figure 2.2a illustrates a schematic of a DAS setup, including laser tuning, gas absorption, and detection[23]. The laser is tuned via current scanning to sweep across a range of optical frequencies ($\nu(t)$). This tuning generates a modulated intensity profile $I_0(t)$, which is partially absorbed by the target gas as it travels through the gas cell. The transmitted signal $I_t(t)$ is then detected and post-processed.

A key output of this process is the absorption coefficient α, which can be derived from the difference between the baseline signal I_0 and the detected intensity I_t. This coefficient is then fitted against known spectra to estimate thermodynamic properties such as temperature (T), pressure (P), and mole fraction (X) of the absorbing species.

Figure 2.2b shows the resulting absorption profile[19]. As the laser scans across a spectral range, light intensity decreases at the absorption line, which reflects where the target gas absorbs most strongly.

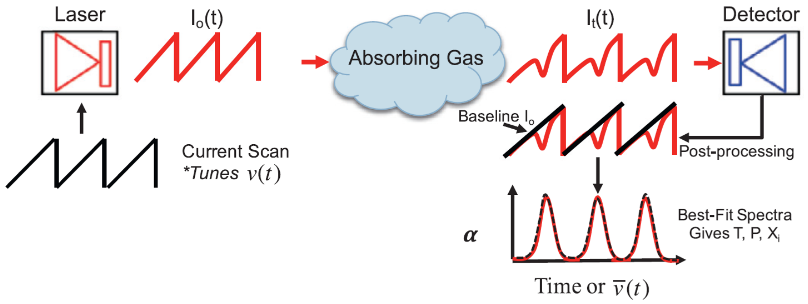

(a) Schematic of a DAS system showing laser tuning, gas absorption, and detection.

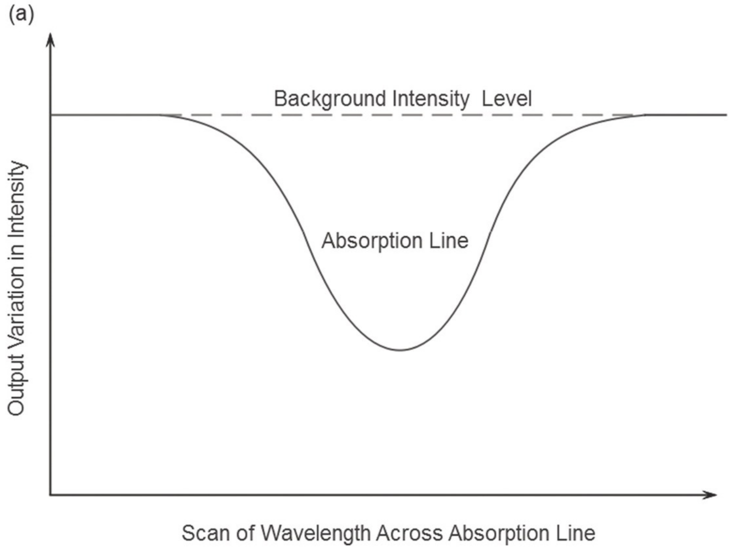

(b) Measured intensity profile indicating how laser light is absorbed at specific wavelengths by gas molecules.

Figure 2.2: Schematic and absorption profile for a DAS system. The resulting spectra can be used to determine gas temperature (T), pressure (P), and species molar fraction (X), which represents concentration.

These visualizations help explain how wavelength-dependent absorption is used to extract gas concentration data from optical measurements. However, this absorption-induced intensity change is often very small compared to the large optical signal, which causes the signal to be overwhelmed by the background noise. While this limits the practical sensitivity of DAS in trace gas detection, its relevance to this thesis lies in its direct application of the Beer-Lambert Law.

DAS provides a clear physical example of how transmission loss relates to gas absorption through path-integrated concentration, making it especially suitable for simulation-informed calibration and algorithm development, as pursued in this study.

.

2.2.2 Wavelength Modulation Spectroscopy

WMS is an analytical technique used to measure trace gas concentrations with improved sensitivity, high selectivity , and reduced noise compared to DAS [19]. In WMS, the laser wavelength is modulated over a controlled range, centered around a known absorption line of the target gas (e.g., methane) which enables the measurement of the absorption characteristics in the IR spectrum[19].

Figure 2.3a illustrates the schematic of a typical WMS system, where the laser wavelength is controlled by two inputs[23]: a slow current scan at frequency f_s, which gradually shifts the average center wavelength λ_0, and a high-frequency sinusoidal modulation at f_m, which causes the wavelength to oscillate rapidly around λ_0. This results in a time-varying laser wavelength defined by:

$$\lambda(t) = \lambda_0 + \Delta\lambda sin(\omega_m t) \tag{2.6}$$

Over a short time interval, where λ_0 can be considered constant, this oscillation enables the laser to scan across the absorption line of the gas, as shown in Figure 2.3b, generating a modulated intensity signal suitable for harmonic analysis in WMS systems[19].

Harmonic Analysis in WMS

As the modulated laser beam passes through the gas sample, the laser wavelength oscillates around the absorption peak. This will result in a periodic variation in the transmitted signal due to variation in gas absorption across different wavelengths[19]. The resulting periodic modulated signal generates components at the fundamental modulation frequency ω_m and its harmonics $2\omega_m, 3\omega_m$, etc. These harmonics can be analyzed and isolated through Fourier decomposition.

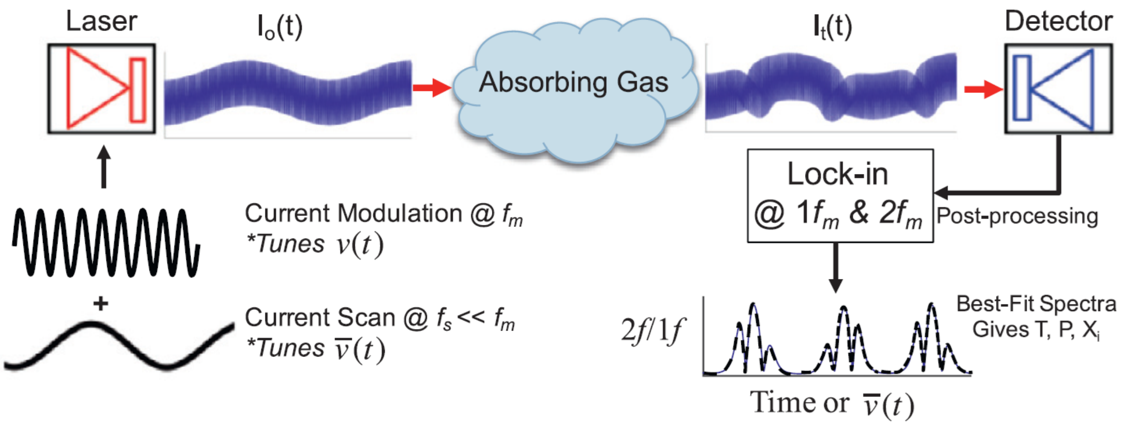

(a) Schematic of a WMS system showing laser modulation, absorption by the gas, and harmonic detection using lock-in amplification.

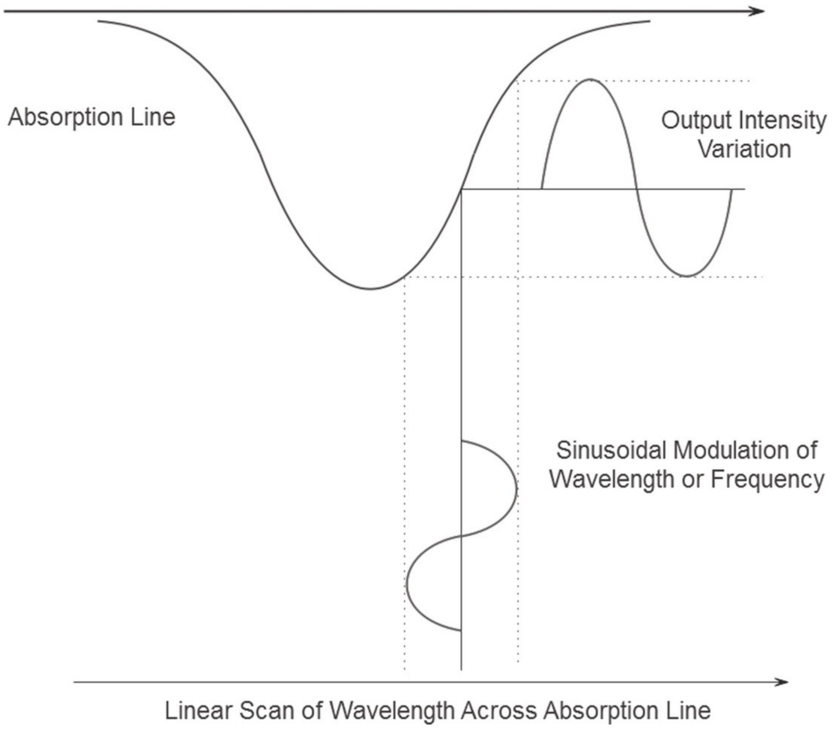

(b) Illustration of how wavelength modulation leads to variation in detected intensity as the laser scans across a gas absorption feature.

Figure 2.3: Wavelength Modulation Spectroscopy (WMS): system schematic and absorption signal variation.

The first harmonic (1f) component typically reflects the overall absorption profile but often carries significant background noise. In contrast, the second harmonic (2f) and higher order harmonics are particularly more robust to detect weak absorption features, as they are inherently much less affected by background noise. This arises from the non-linear interaction between the laser modulated wavelength and the gas absorption line, which enhances contrast and improves the signal-to-noise, making WMS effective for the sensitive detection of weak absorption features[19, 23].

Phase Sensitive Detection with Lock-in Amplification

A primary challenge in WMS is the extraction of weak harmonic signals while buried in noise. To address this, a phase-sensitive method known as lock-in amplification is commonly used[19]. In this technique, the detected signal is multiplied by a reference signal (f_r) , usually at the same modulation frequency (e.g., $f_s = f_r = f$) as shown in Figure 2.4, through a mixer[24].

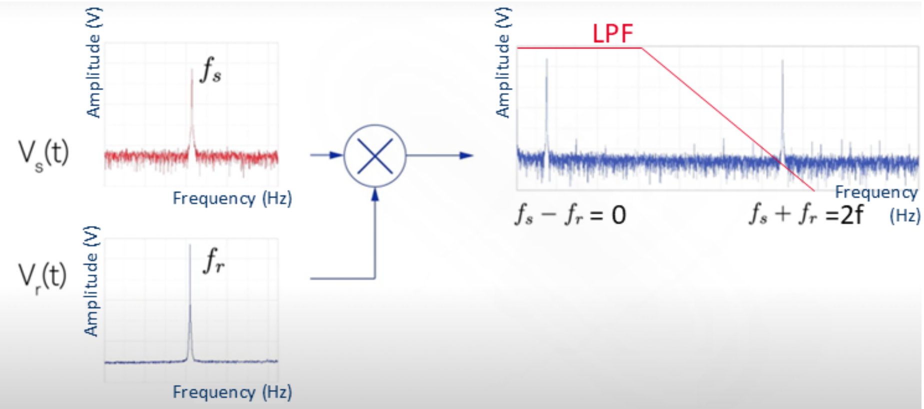

Figure 2.4: Frequency-domain illustration of harmonic signal extraction via lock-in detection.

This multiplication yields components at the difference and sum of the source and reference frequencies (e.g., $f_s \pm f_r$)[24]. This process generates output components at DC (0 Hz) and the target harmonic frequency (e.g. 2f) appear as peaks in the frequency domain. The desired harmonic, typically 2f, is then isolated using low-pass filter (LPF) or band-pass filter(BPF), while filtering out other frequency components and noise. The filter is commonly built into the lock-in amplifier[24].

By adjusting the reference frequency, different harmonics (e.g., 2f or 3f, etc.) that are free from or have minimal background noise can be extracted, providing highly stable absorption signals. This selective filtering isolates the modulated absorption signal from background noise, greatly improving measurement sensitivity.

Advantages of WMS

WMS offers advantages over other absorption techniques such as DAS. While both methods can employ lock-in detection to improve sensitivity, WMS specifically modulates the laser wavelength at a known frequency, allowing harmonic extraction with intrinsically low or zero background levels. This results in an improved signal-to-noise ratio and makes WMS particularly well suited for reliable absorption measurements in low-concentration environments. In addition, WMS is robust against various sources of noise , making it a powerful tool for real-time, on-site monitoring of gases such as methane.

Overall, this modulation technique utilizes the strong absorption features of gases at specific wavelengths to detect even small changes in the output-to-input power ratio $\frac{\Delta P}{P_{in}}$, allowing the precise detection of low-concentration gases using their spectral signatures. The resulting absorption signal reflects the difference between the background (off-line) intensity and the gas absorption at specific wavelengths, which provides the basis for determining the presence and concentration of gases such as methane.

Relevance to This Study

In the context of this thesis, WMS is considered from a conceptual perspective, as it reflects how absorption-based systems relate transmission loss to gas concentration along the optical path. The principle of using harmonic detection and integrated absorption parallels the simulation-informed framework developed later in this study, where concentration fields are projected into optical analogs for methane leak quantification.

2.2.3 Frequency Modulation Continuous Wave

FMCW is a laser-based metrology technique traditionally used for range measurements, in which a continuous wave (CW) signal is modulated in frequency over time [25]. The continuous nature of the FMCW signal enables uninterrupted transmission, allowing for high-resolution and real-time distance estimation, which is particularly valuable in applications such as autonomous navigation and surface profiling[25].

In many implementations, FMCW systems are integrated into fiber-based optical setups, where a frequency-modulated laser beam is directed toward an environment of interest. One such specialized application is commonly referred to as FMCW light detection and ranging (Lidar) which transmits a frequency-modulated signal typically toward an object. Figure 2.5a shows a typical configuration of an FMCW

Lidar system.

The returned signal, after interacting with the object is mixed coherently with local oscillator (LO) as a reference beam to extract the intermediate frequency (IF) which contain distance information.

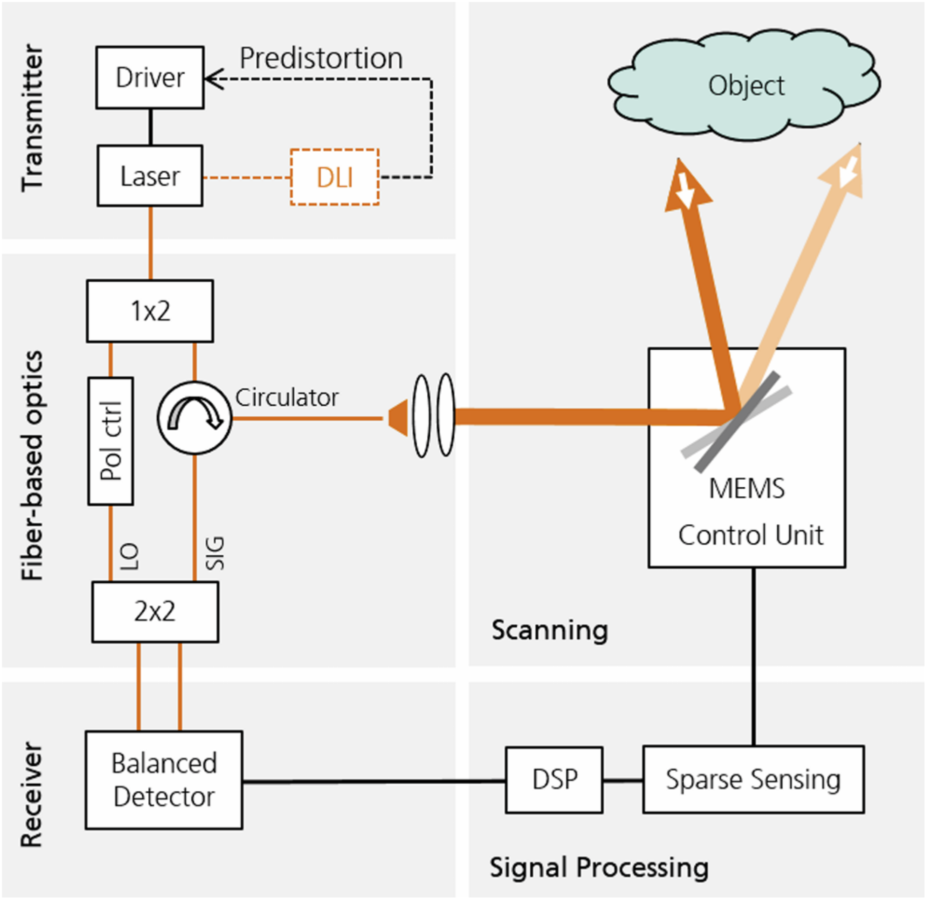

(a) Schematic of an FMCW Lidar system showing transmitter, receiver, and optical mixing for signal processing. A continuous-wave laser is modulated and split into signal and reference paths. The signal is directed toward the target via a MEMS scanner; the reflected light is mixed with the reference at the balanced detector to extract frequency shifts

[25]

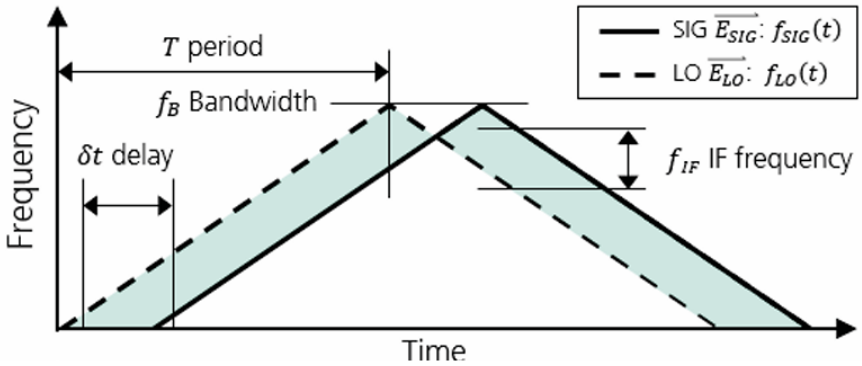

(b) Frequency-time diagram showing linear frequency modulation, delay, and the resulting intermediate frequency used for distance . [25]

Figure 2.5: FMCW Lidar system and modulation principle for range analysis.

In such a system, a continuous-wave laser signal is directly frequency modulated across a bandwidth f_B over a time period T, commonly in a linear chirp pattern, where the frequency linearly increases or decreases with time. This modulated signal is transmitted to the target and interacts with the object. The received signal is delayed by a time δt and exhibits a frequency shift relative to the LO, known as the intermediate frequency f_{IF}.

With appropriate modifications such as incorporating spectral encoding, the principles of FMCW can also be adapted for spectroscopic gas sensing[13]. Such approach has the potential to enable simultaneous measurement of gas concentration and range, offering a powerful approach for environmental monitoring and methane leak detection.

As shown in Figure 2.5b, this frequency shift is generated by mixing the delayed signal with the LO at the detector. This intermediate frequency is proportional to the round-trip distance. In modified systems that incorporate spectroscopic analysis, gas absorption can be observed as amplitude changes at specific frequencies.

Compared to traditional WMS, which applies modulation at a fixed wavelength, a modified FMCW approach can simultaneously provide spatial information (via frequency chirps) and spectral information (via absorption features). This makes it ideal for applications where combined distance and gas concentration information is needed.

The FMCW Lidar system is widely used to measure distance and velocity in applications such as self-driven cars [19][25], and more pertinently to this study, FMCW Lidar has a significant potential, when appropriately modified, for atmospheric gas analysis including methane detection[13][26].

Advantages of FMCW

- Real-time monitoring: Unlike traditional pulsed systems , FMCW systems provide continuous and dynamic measurements, aiming to sustain a high duty cycle, which is essential for applications like environmental monitoring and leak detection.

- High sensitivity : In FMCW systems high sensitivity arises from the principle of coherent (heterodyne) detection, in which a weak received optical signal is mixed with a strong LO field at the photodetector. This process shifts the signal information to a higher intermediate frequency (IF)[25][27], where noise is lower and small frequency variations caused by distance or gas absorption can be resolved with high precision. As a result, FMCW heterodyne detection enables accurate measurement of very weak optical signals [27].

The optical fields of the received signal and the local oscillator can be written as

$$E_{sig}(t) = A_s e^{-i(\omega_s t + \phi_s)}, \quad E_{LO}(t) = A_{LO} e^{-i(\omega_{LO} t + \phi_{LO})},$$

where A_s and A_{LO} are the field amplitudes, ω_s and ω_{LO} are the optical angular frequencies, and ϕ_s and ϕ_{LO} are the corresponding phases [27]. The average optical powers are related to the field amplitudes by $P_{sig} = A_s^2$ and $P_{LO} = A_{LO}^2$ [27].

The total detected optical field is[27]

$$E(t) = E_{sig}(t) + E_{LO}(t),$$

and the corresponding detected power becomes

$$P(t) = |E(t)|^2 = P_{sig} + P_{LO} + 2\sqrt{P_{sig} P_{LO}} \cos(\Delta\omega t + \Delta\phi),$$

where $\Delta\omega = \omega_s - \omega_{LO}$ and $\Delta\phi = \phi_s - \phi_{LO}$. The third term represents the heterodyne (beat) component carrying the frequency and phase information of the received signal, producing an AC photocurrent proportional to $2\sqrt{P_{sig} P_{LO}}$ [27].

Because $P_{LO} \gg P_{sig}$, the mixing process effectively amplifies the weak signal before electrical detection. Thermal and electronic noise remain nearly constant with increasing P_{LO}, while the signal amplitude grows as $\sqrt{P_{LO}}$, leading to an improvement in signal-to-noise ratio (SNR). This coherent mixing gain enables FMCW systems to detect extremely weak reflections with high sensitivity and precision.

In contrast, direct detection measures only the signal intensity $|E_{sig}|^2 = P_{sig}$, producing a photocurrent proportional to P_{sig}. Since no strong local oscillator is used, there is no heterodyne term to enhance the signal, and the detected power remains very small. Therefore, coherent heterodyne detection offers a significant SNR advantage over direct detection by introducing the large interference term $2E_{sig}E_{LO}$, which acts as an effective optical amplification mechanism.

- Multi-sensing capabilities: When combined with spectroscopic techniques, FMCW

Lidar systems can in principle extract distance, gas concentration, and even wind speed[28], offering a potential path toward comprehensive environmental monitoring.

Conclusion

FMCW Lidar combines precise range measurement with the potential for real-time gas detection when spectral encoding and coherent detection techniques are incorporated. Its ability to encode both spatial and spectral information makes it a promising approach for methane leak detection and quantification, especially in dynamic or open environments. With further development, such systems could play an important role in managing and mitigating methane emissions, contributing to both scientific research and environmental sustainability.

As a result, FMCW Lidar plays a crucial role in managing and mitigating methane emissions, contributing to both scientific research and environmental sustainability.

Relevance to This Study

In this study, methane quantification relies on the optical absorption of laser light by the Beer-Lambert Law. Simirlar to WMS and DAS, FMCW Lidar uses this principle and serves as a conceptual model for a detection technique, but it also has the potential to provide high-sensitivity measurements of gas parameters under appropriate system modifications.

The combination of spatial resolution (via frequency shift) and gas-specific absorption (via spectral features) enables simultaneous localization and quantification of methane concentrations and reflects the foundational idea behind the simulation methods developed later in this thesis, offering a powerful way to track methane in real time.

2.3 Imaging-Based Optical Gas Sensing Techniques

While the techniques described so far rely on laser-based point sensing, imaging-based systems such as OGI cameras and scanning Lidars offer the ability to visualize gas dispersion across a spatial scene [17]. These systems also rely on the Beer–Lambert Law, measuring integrated path absorption along the line of sight rather than at a single beam.

An OGI setup, such as the schematic illustrated in Figure 2.6, uses an infrared camera (e.g., FLIR GF77) to visualize gas plumes by detecting radiance contrast in a spectral band where methane absorbs, against a contrasting background structure. The ability to detect the plume depends on the net effective temperature difference between the background and the gas integrated path absorption, which must be sufficient for reliable visualization [17][29].

However, conventional imaging tools often lack the capability for accurate quantification due to challenges such as background clutter, low signal strength, and the inability to resolve gas composition in mixtures[16]. OGI cameras, in particular, are sensitive to temperature contrast and gas opacity, but not directly to concentration.

In this study, a simulation-based framework is developed to replicate the measurable outputs of such imaging systems, including camera-like visualizations or integrated absorption maps. This approach enables quantitative leak assessment from simulated optical projections and bridges the gap between 3D gas dispersion modeling and real-world sensor responses.

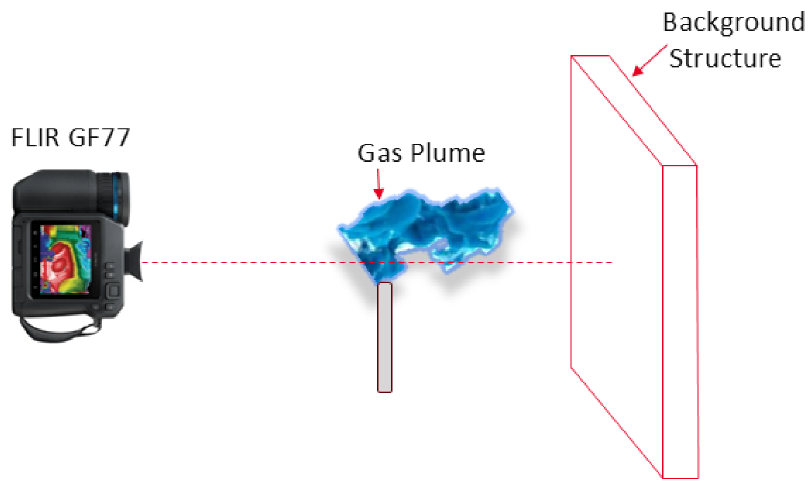

Figure 2.6: Schematic representation of an Optical Gas Imaging (OGI) setup using a FLIR GF77 camera. The infrared camera captures the gas plume as it absorbs background infrared radiation, with the background structure providing necessary contrast for plume visibility.

2.4 Fundamentals of Fluid Flow

This section introduces fundamental concepts of fluid dynamics that form the theoretrical foundation for CFD. Topics covered include system and control volume concepts, flow regimes, compressibility, and conservation laws. These core concepts are crucial for understanding and modeling complex fluid systems, including those encountered in leak detection and quantification.

2.4.1 Fluid

A fluid is defined as any substance that can easily deform when a force is applied, implying that it does not have a fixed shape. Fluids include both liquid and gas, and tend to flow and conform to the shape of their container. Unlike more rigid materials(e.g. solids), they can be continuously deformed without resistance as long as the force persists and the volume remains unchanged[30]. Additionally, fluids may be compressible or incompressible, depending on the conditions and assumptions applied in a given analysis; for example, air flowing at supersonic speeds is treated as compressible, while air at low speeds is often approximated as incompressible.

2.4.2 Fluid Dynamics

Fluid dynamics is the study of how fluids move and how forces affect that motion and explains their behavior under dynamic conditions [31]. Understanding the principles of fluid dynamics is essential in various engineering applications, including pipeline design and leak detection.

Improving the performance of systems that operate using fluids requires a comprehensive analysis of how fluids flow and behave. Fluid motion is governed by a number of fundamental conservation rules, which guarantee that mass, momentum, and energy are maintained in all systems.

In this section, the primary focus will be on the conservation of mass, commonly expressed through the continuity equation, as it provides the foundational understanding of how fluid behaves when moving through space. This emphasis is especially important for scenarios involving gas transport or leakage, where accurate tracking of how the mass enters, exits, or accumulates is critical.

2.4.3 System and Control Volume

To systematically analyze how mass is transported a given region, we need a framework that supports this. This is where the concept of a system (material volume) and control volume becomes essential, providing a basis for deriving fundamental conservation laws[32].

A system is a collection of a fixed, identifiable quantity of mass[32][33]. On the other hand, a control volume (CV) is an arbitrary and well-defined volume in space through which fluid may flow[32][33]. These two volume concepts are shown in figure 2.7 [33].

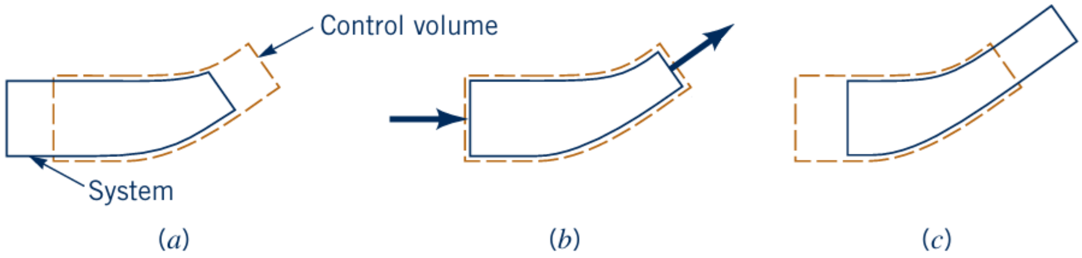

Figure 2.7: System and control volume at three different instances of time. (a) System and control volume at time $t-\delta t$. (b) System and control volume at time t, coincident condition. (c) System and control volume at time $t+\delta t$.

The geometric boundary of the control volume is known as the control surface. This surface can be either real (such as physical walls of a pipe) or imaginary (e.g., at inlet or outlet boundaries). In the illustrative figure 2.8 [32], both real control surfaces (pipe walls corresponding to top and bottom boundary) and imaginary control surfaces (inlet and outlet) are shown for a narrowing pipe.

The control volume approach allows us to analyze the movement and accumulation of mass, energy, or momentum within a system. Conservation laws can be formulated over infinitesimally small (for local behavior) or finite-sized volumes (for system-level analysis). These two approaches are complementary, and both are explored later in this thesis to describe conservation laws differentially and integrally and to simulate fluid behavior[32].

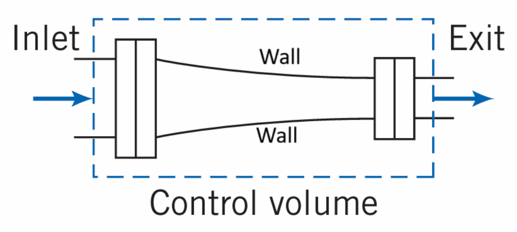

Figure 2.8: Control volume and control surfaces of a narrowing pipe flow. The pipe walls represent real control surfaces, while the inlet and outlet boundaries define imaginary control surfaces.

2.4.4 Laminar vs Turbulent Flow

The fluid can exhibit distinctly different behaviors depending on flow conditions. These behaviors are broadly classified as laminar, transitional, or turbulent flow regimes. In laminar flow, fluid particles move in smooth, orderly layers with minimal mixing between them. In contrast, turbulent flow is characterized by chaotic velocity fluctuations and vigorous mixing due to the presence of eddies, which are localized swirling motions in the fluid. Transitional flow lies between these two extremes, where the flow exhibits intermittent instability, sometimes appearing laminar and at other times becoming turbulent.

These flow regimes were first systematically studied by Osborne Reynolds in the 19th century[33]. In his famous experiment, water was made to flow through a transparent pipe while a dyed filament was introduced at the centerline. At low velocities, the dye remained a thin, straight line, indicating laminar flow shown in Figure 2.9a. As the velocity increased, the dye began to oscillate and eventually broke into a diffuse, erratic pattern which signals a transition to turbulence.

Figure 2.9b illustrates how the fluid velocity measured at a point in the volume varies over time in each regime: remaining constant in laminar flow, showing intermittent variations in transitional flow, and fluctuating unpredictably in turbulent flow.

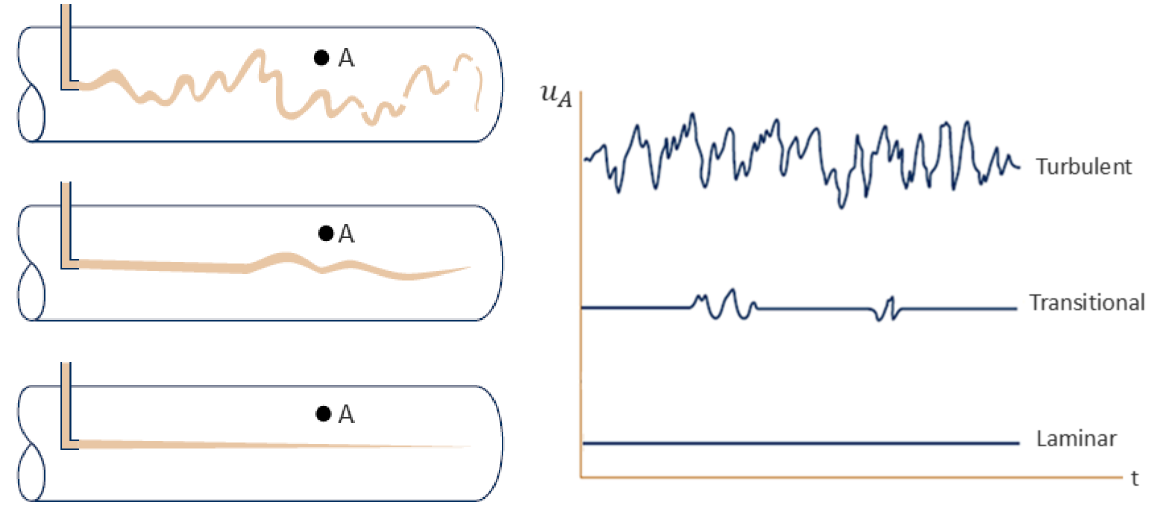

(a) Visualization of laminar and turbulent flow using dye injection in a pipe[33].

(b) Velocity fluctuations over time for laminar, transitional, and turbulent flows[33].

Figure 2.9: Visualization of flow regimes: dye streamlines and velocity fluctuation patterns.

Further analysis by Reynolds showed that flow regime depends not only on the velocity V, but also on other parameters such as fluid density ρ, viscosity μ, and a characteristic length scale L (typically the pipe diameter). These were combined into a single dimensionless number, now known as the Reynolds number (Re):

$$Re = \frac{\rho V L}{\mu} \tag{2.7}$$

Typical thresholds for defining these flow regimes are that laminar flow occurs when $Re \leq 2100$, turbulent flow when $Re \geq 4000$ is turbulent. and values between these limits $2100 < Re < 4000$ are considered transitional[33].

Understanding these regimes is essential in fluid modeling, especially when simulating gas dispersion. In this study, turbulent flow conditions are of particular interest because of their relevance in real-world methane leak scenarios, where velocity fluctuations strongly influence dispersion.

2.4.5 Compressible vs Incompressible Flow

In fluid dynamics, flow is considered incompressible if the fluid density remains constant throughout its motion. A compressible flow, on the other hand, is when the fluid density varies significantly, typically due to changes in pressure, which is particularly common in gas flows.

For gases such as methane, compressibility should theoretically be taken into account because gases are highly sensitive to pressure variations. However, in many practical situations, especially those involving low-speed flows or small pressure drops, these density changes are negligible. In such cases, it is common and acceptable to assume incompressible behavior as a simplifying approximation.

In this study, the carrier gas (air) is treated as incompressible because the flow velocities are in the low-Mach regime ($Ma < 0.3$). However, methane transport is solved using a species conservation equation, which allows the local mixture composition, and hence the mixture density, to vary in space and time. This distinction ensures that plume dispersion and dilution are captured accurately while maintaining the computational efficiency of an incompressible flow solver.

In this research, air flow is solved under the incompressible flow assumption, which is valid for the low-speed conditions considered ($Ma < 0.3$). The methane concentration field is solved using the species transport equation, which accounts for both advection and diffusion. This treatment allows the local mixture composition, and consequently the mixture density, to vary in space and time. In this way, plume dispersion is captured accurately while still treating the carrier gas (air) as incompressible, consistent with the low-Mach-number flow assumption. The species transport equation governs the evolution of methane concentration in the domain, and its solution modifies the local mixture density, enabling correct modeling of gas dispersion and dilution.

However, in situations involving large leaks, high velocities, or significant pressure differences, the effects of compressibility become more pronounced. In such cases, incompressible assumptions will introduce errors, and a full compressible analysis becomes necessary for accurate modeling.

Compressibility can be evaluated using the dimensionless Mach number (Ma), which compares the flow speed to the speed of sound in the medium. For $Ma < 0.3$, flow can typically be treated as incompressible[32].

2.4.6 Conservation Laws in Fluid Dynamics

The conservation laws of fluid dynamics form the basis for understanding fluid behavior in different situations [30][31]. They consist of the conservation of mass, momentum, and energy. Each law can be expressed in both integral and differential forms, where the integral form applies to finite control volumes and the differential form focuses on local, point-wise behavior [30][31].

For the purpose of this research, the focus is on the mass-conservation law in both its differential and integral forms. This principle provides the theoretical basis to analyze fluid motion in leak detection scenarios and enable precise quantification of gas concentrations and flow rates.

The Continuity Equation (Mass Conservation)

The conservation of mass is mathematically expressed by the continuity equation, which states that the total mass within a given system (or material volume) remains constant, shown as:

$$m = \int_V \rho \, dV \tag{2.8}$$

Here, $V = V(t)$ represents a moving system volume. Because no mass is created or destroyed within the fluid system, the rate of mass over time must be zero as follows[31]:

$$\frac{Dm}{Dt} = \frac{D}{Dt}\int_V \rho \, dV = 0 \tag{2.9}$$

Integral Form of Mass Conservation To relate the system perspective to a fixed control volume, we apply the Reynolds Transport Theorem (RTT) [31][33][34], which transforms the material derivative (equation 2.9) into a form that accounts for the rate of change of mass within a control volume (local accumulation) and the mass flux across its boundary as follows:

$$\frac{D}{Dt}\int_V \rho \, dV = \int_V \frac{\partial \rho}{\partial t} dV + \int_{\partial V} \rho \mathbf{V} \cdot d\mathbf{A} \tag{2.10}$$

2.21 where

- ρ is the fluid density,
- $\mathbf{V}$ is the velocity vector of the fluid at the boundary,
- $d\mathbf{A}$ is an infinitesimal outward-pointing area vector on the control surface ∂V, and
- V denotes the control volume

which yields the integral form of mass conservation:

$$\int_V \frac{\partial \rho}{\partial t} dV + \int_{\partial V} \rho \mathbf{V} \cdot d\mathbf{A} = 0 \tag{2.11}$$

In many practical applications, specially those involving fluid transport and leak detection, the integral form is particularly valuable. It directly accounts for how mass flows into and out of a finite control volume without requiring detailed information at every internal point.

Considering a control volume V with control surface S, the integral form of mass conservation can be expressed as[31][32]:

$$\int_V \frac{\partial \rho}{\partial t} dV + \int_{\mathbf{S}} \rho \mathbf{V} \cdot d\mathbf{S} = 0 \tag{2.12}$$

Steady Flow Condition In a steady fluid flow, fluid properties such as density does not change with time; the first term disappears and the integral conservation of mass equation simplifies to:

$$\int_S \rho \mathbf{V} \cdot d\mathbf{S} = 0 \tag{2.13}$$

This equation states that, under steady conditions, the net mass flux across the control surface must be zero. In other words, the total mass entering the control volume through the inlet must exactly equal the total mass leaving it through the outlet:

$$\int_{\mathbf{S}_{in}} \rho \mathbf{V} \cdot d\mathbf{S} + \int_{\mathbf{S}_{out}} \rho \mathbf{V} \cdot d\mathbf{S} = 0 \tag{2.14}$$

Since the integral equation represents the total mass balance across the control surface, it can be expressed in terms of the mass flow rate, $\dot{m}$, which represents the total mass passing through a surface per unit time and is defined as:

$$\dot{m} = \int_{\mathbf{S}} \rho \mathbf{V} \cdot d\mathbf{S} \tag{2.15}$$

Substituting this expression into the integral equation 2.14, assuming we have an inlet and an outlet, leads to:

$$\dot{m}_{in} = \dot{m}_{out} \tag{2.16}$$

More generally, there could be a number of inlets and outlets so we can rewrite the equations as:

$$\sum \dot{m}_{in} = \sum \dot{m}_{out} \tag{2.17}$$

Differential Form of Mass Conservation In order to obtain the local form of mass conservation, the surface integral in equation 2.11 is converted to a volume integral using the Divergence Theorem:

$$\int_{\partial V} \rho \mathbf{V} \cdot d\mathbf{A} = \int_V \nabla \cdot (\rho \mathbf{V})\, dV \tag{2.18}$$

with which equation 2.10 leads to the equation below[31]:

$$\int_V (\frac{\partial \rho}{\partial t} + \nabla \cdot (\rho \mathbf{V}))\, dV = 0 \tag{2.19}$$

This means that the integral must be zero for any infinitesimally arbitrary small control volume of V. This is only possible if the expression inside the integral itself is zero at every point within that volume. This gives the differential form of the continuity equation, as follows:

$$\frac{\partial \rho}{\partial t} + \nabla \cdot (\rho \mathbf{V}) = 0 \tag{2.20}$$

This point-wise form of mass conservation describes how fluid density and velocity change at each locationin the flow field. It applies to an infinitesimal control volume and is expressed as a partial differential equation, capturing local mass behavior in space and time.

Incompressible Flow Condition Equation 2.20 expresses local mass conservation and applies to both compressible and incompressible flows. However, in incompressible flows, the density of the fluid remains constant along the path of a moving fluid element. The material derivative of density which describes the rate of the quantity(e.g., density) as observed while moving with the fluid is written as [30][31][33][34]:

$$\frac{D\rho}{Dt} = \frac{\partial \rho}{\partial t} + \mathbf{V} \cdot \nabla \rho \tag{2.21}$$

As mentioned earlier, for an incompressible flow, this is zero:

$$\frac{D\rho}{Dt} = 0 \tag{2.22}$$

so material derivative will be:

$$\frac{\partial \rho}{\partial t} + \mathbf{V} \cdot \nabla \rho = 0 \tag{2.23}$$

which, substituted into the differential form (equation 2.20), simplifies to the incompressibility constraint:

$$\nabla \cdot \mathbf{V} = 0 \tag{2.24}$$

This expression indicates that the net volumetric flow into any point must be zero, fully consistent with the behavior of incompressible fluids. In this thesis, this incompressibility constraint is applied to the air flow field, as discussed in Section 2.4.5.

2.5 Numerical Modeling

As mentioned earlier, methane, being a highly potent greenhouse gas, presents significant environmental and climate-related concerns. To mitigate its impact effectively, especially in the case of unintended leaks , it is essential to identify the leak source and understand how the released gas disperses in the atmosphere. Once these are established, the next significant step is to quantify the amount of gas released to accurately assess its environmental consequences and ensure timely intervention.

However, direct field measurements are often difficult to perform due to high costs, logistical constraints, and the influence of various factors such as wind, terrain, and atmospheric variability. In this context, numerical modeling offers a practical and robust alternative. It provides simulation of real-world leak scenarios under controlled repeatable conditions, where key variables such as wind speed, leak size, and ambient properties can be systematically adjusted. This allows for qualitative analysis of the dispersion behavior, evaluation of concentration fields, and ultimately quantitative estimation of methane leak rates.

Modeling plays a crucial role in gas leak analysis, serving as the primary tool for understanding leak behavior, optimizing leak detection strategies, and improving system design. Additionally, one of the key advantages of simulation is its ability to test multiple scenarios efficiently under a wide range of controlled environmental conditions. These investigations are repeatable and consistent, which overcomes the unpredictability of physical experiments.

2.5.1 Computational Fluid Dynamics (CFD)

CFD is a subfield of fluid mechanics that applies numerical methods to analyze and simulate fluid flow behavior. It solves the governing equations of fluid motion using discretized iterative methods [32]. Instead of generating closed-form equations, CFD represents fluid behavior using numerical approximations obtained by discretizing the computational domain on a grid or mesh [32]. This cabability makes CFD a powerful tool for complex dynamic scenarios such as gas leak studies under varying conditions, where real-world variability makes analytical solutions impractical.

COMSOL Multiphysics

There are several CFD simulation tools available such as Ansys Fluent, COMSOL Multiphysics, and OpenFOAM, commonly used for fluid flow simulation. Among them, COMSOL Multiphysics stands out for its ability to model complex multiphysics interactions within a single environment. As the name implies, it integrates multiple modules, including fluid dynamics, heat transfer, and species transport, making it highly suitable for studying gas leaks and dispersion.

COMSOL employs Finite Element Method (FEM), which provides high precision in solving multi-physics problems. Unlike Finite Volume Method (FVM) used in some other tools like Fluent, FEM discretizes complex geometries and sharp gradients more precisely, particularly in coupled phenomena. It captures a detailed resolution of variations within the domain while minimizing numerical error. As a result, FEM enables more accurate simulations, which makes COMSOL particularly strong for fluid dynamics problems under diverse conditions.

Another advantage is COMSOL's built-in meshing. Many CFD software packages require external meshing tools, which can complicate the workflow. In contrast, COMSOL generates and refines meshes inside the same environment, which makes the entire simulation process smoother and more efficient.

Given these benefits, COMSOL was chosen for this study to simulate methane gas leaks into the atmosphere. Its ability to efficiently test multiple realistic scenarios in a controlled, repeatable environment helps refining conditions and identifies the optimal case before conducting costly and time-consuming laboratory or field experiments.

The general workspace of COMSOL used for this model is shown in Figure 2.10.

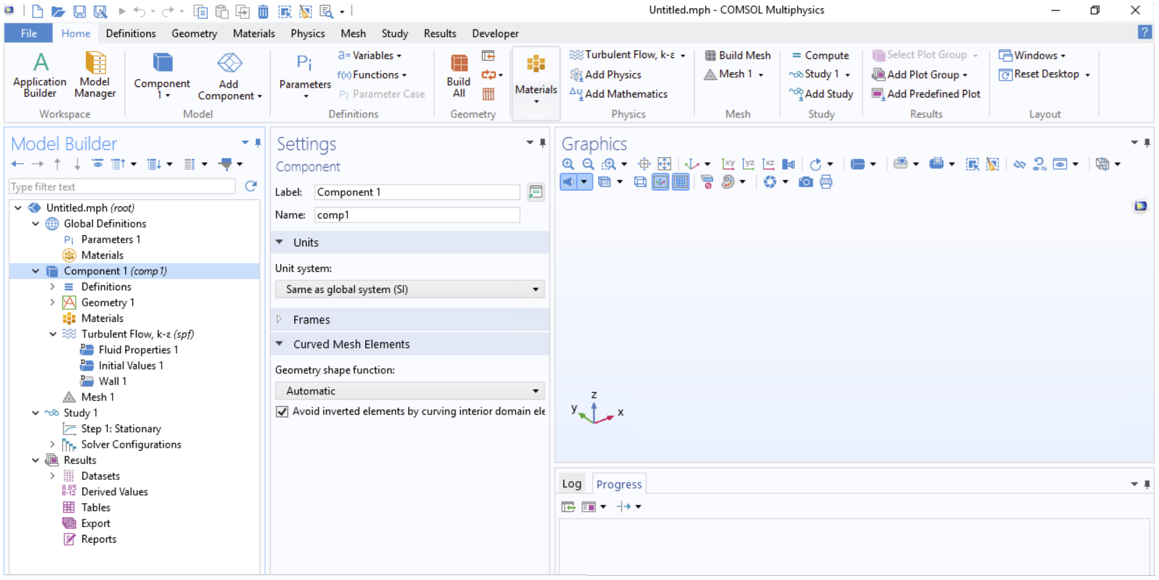

Label: Component 1

Name: comp1

Unit system: Same as global system (SI)

Geometry shape function: Automatic

☑ Avoid inverted elements by curving interior domain ele

Figure 2.10: COMSOL Multiphysics user interface showing the model builder, settings window, and graphics view used in the simulation workflow.

The workspace is divided into three primary panels that streamline the modeling process:

Model Builder (Left Panel): Displays a tree-like structure that provides an intuitive layout and organizes the model step-by-step from defining global definitions to geometry, physics, mesh, solver configuration, and results.

Settings Window (Center Panel): Displays editable settings based on the selected item in the model builder. This is where model parameters, materials properties, and solver settings are applied.

Graphics Window (Right Panel): Represents visual model components such as geometry, mesh, and simulation results which allows for interactive exploration of the model.

Additional interface tabs such as Messages, Progress, and Log at the bottom provide useful feedback during the simulation process.

Chapter 3

Simulation Methodology and Implementation

3.1 Model Definition

This chapter presents the numerical simulation of a methane leak from a small, pipe-like source in an open-air environment. The objective is to analyze how methane disperses into the environment, particularly for low emission rates of such as 100 g/h, and 1000 g/h, under simplified but controlled environmental conditions such as ambient wind.

Understanding the spatial behavior of the methane plume, including how it evolves and stabilizes over distance, is essential for developing effective leak detection and quantification strategies. This becomes particularly important at low methane leak rates, where the observable concentration signal may be weak and the dispersion is highly sensitive to environmental factors such as wind and atmospheric conditions.

To realistically simulate this behavior, it is necessary to model both fluid flow and mass transport phenomena in a coupled manner [22, 33] . Specifically, the model must solve the Navier-Stokes equations (which govern the air and methane flow dynamics, including momentum and velocity fields) alongside the mass transport equations (which track the concentration of methane in air).

This coupling ensures that the interaction between the jet momentum, turbulence, and atmospheric dispersion is captured accurately. A more detailed explanation of the governing equations and their implementation will be provided in the following sections.

To achieve this, a 3D simulation model is developed using COMSOL Multiphysics. The modeling process requires a proper setup, including defining the geometry, material properties, physics module selection, boundary conditions and generating an appropriate mesh, followed by solving the computational problem. Each of these steps directly influences the simulation's accuracy and the reliability of the results.

The following sections describe each phase of the model-building process in detail, with the goal of closely representing realistic methane leak scenarios into the atmosphere.

3.2 Geometry Setup

The geometry used in this simulation represents a simplified open-air domain, carefully designed to balance realism and computational cost. As shown in Figure 3.2, the simulation space is modeled as a rectangular 3D domain measuring 2 m × 2 m × 2 m, a size sufficient to reduce artificial boundary effects and allow full development of methane plume.

In real-world oil and gas production sites, methane emissions can originate from a range of surface components such as valves, tank hatches, vents, and exhaust stacks, as shown in Figure 3.1 [35]. These typical leak sources are not necessarily connected to underground pipelines, but often arise from above-ground infrastructure where gas is released directly into the atmosphere. Modeling a vertical stack as the leak source in this study therefore represents a practical and realistic emission scenario consistent with common field observations.

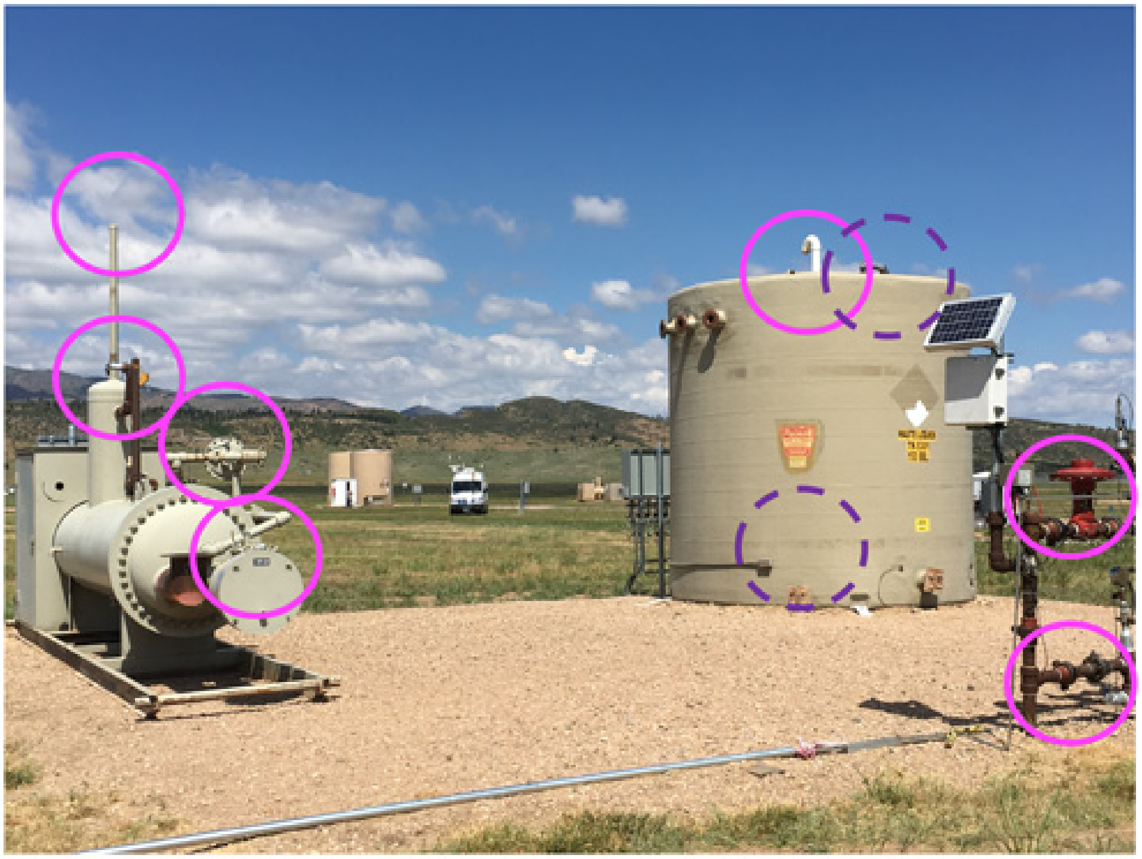

Figure 3.1: Typical methane leak locations in an oil and gas facility

Accordingly, in this model,the methane leak is introduced through the open top surface of a small vertical circular pipe, placed on the ground. The pipe extends 0.5 meters vertically along the z-axis and is located at y=0.8 (m) to ensure sufficient downstream space for plume development. This configuration mimics a realistic small-scale leak, allowing for both vertical buoyant rise and horizontal transport influenced by ambient wind conditions.

This representative geometry setup defines the computational domain for the simulation. It is large enough to capture the development of the methane plume, both near the source and farther downstream, while maintaining computational feasibility. The domain provides sufficient resolution to resolve concentration gradients at different leak rates which makes it appropriate for detailed post-processing and quantitative leak rate analysis.

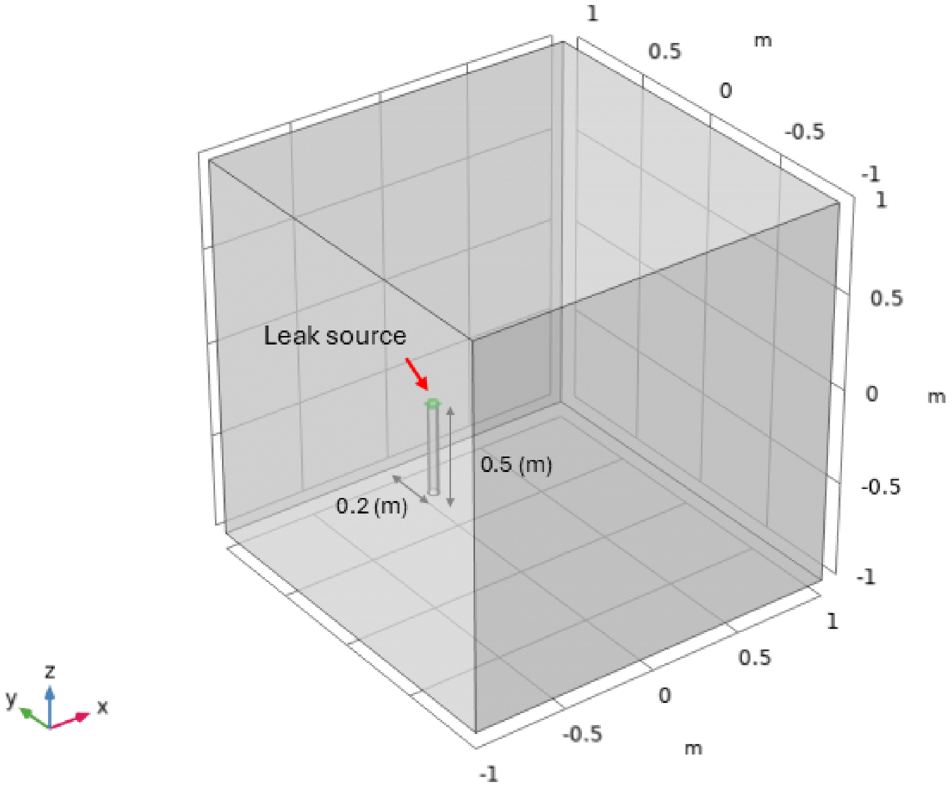

Figure 3.2: 3D simulation domain representing open-air environment.

3.3 Material Definition

Material properties play a key role in determining how gases behave once released into the atmosphere. Properties such as density, viscosity, and diffusivity directly influence the movement, mixing, and dispersion patterns of methane in the surrounding environment. Since this study focuses on methane leaking into ambient air, accurate definition of material properties for both methane and air is essential for reliable and physically meaningful simulation results.

Methane (CH_4) is the gas studied in this study. In this model, methane material properties were sourced directly from the COMSOL material library to improve accuracy and ensure the model reflects real-world behavior.

Each of methane's material property plays a crucial role in gas dispersion behavior: Being lighter than air, methane tends to rise due to buoyancy effects governed by its density. Viscosity influences the internal friction of the gas, affecting how smoothly it mixes with the surrounding air and contributes to momentum diffusion. Diffusivity determines how fast methane molecules spread across concentration gradients within the airflow.

Since methane disperses into air, it is equally important to define the material properties of the surrounding medium, air. Table 3.1 presents a comparison between the relevant properties of methane and air under standard conditions.

Air acts as the surrounding environment through which methane spreads. Its density, viscosity, and molecular diffusivity directly impact the movement of the plume, whether it rises, forms turbulent patterns, remains near the leak source, or rapidly dilutes into the surroundings. As with methane, the properties of air were taken from the COMSOL built-in material library to maintain accuracy and consistency with real-world conditions.

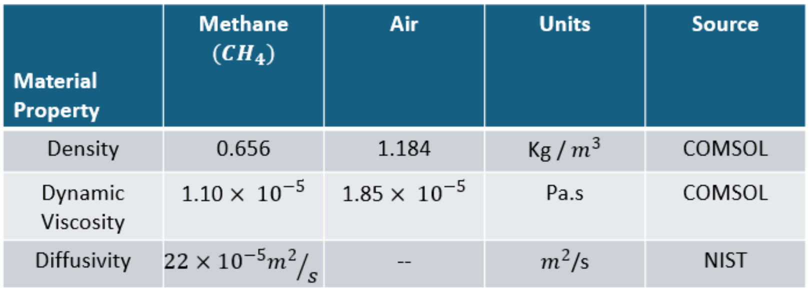

Material Property	**Methane (CH_4)**	**Air**	**Units**	**Source**
Density	0.656	1.184	Kg / m^3	COMSOL
Dynamic Viscosity	1.10×10^{-5}	1.85×10^{-5}	Pa.s	COMSOL
Diffusivity	$22 \times 10^{-5} m^2/s$	--	m^2/s	NIST

Table 3.1: Material properties of methane and air at 1 atm and 25 °C.

For this study, material properties were defined under standard atmospheric conditions (1 atm, 25°C) to represent typical environmental conditions. While temperature variations can influence material properties and, consequently, dispersion patterns, their impact was assumed negligible and constant for this study to focus on leak rate and environmental effects. As such, temperature dependency was not a focus of this work.

3.4 Physics Framework and Governing Equations

To accurately model methane leaks and their dispersion in the air under various wind conditions, appropriate physics interfaces have been selected in COMSOL. As discussed in the modeling workflow in Section 3.1, this model involves both fluid flow and chemical transport of species, which is accomplished using two primary physics interfaces:

- **Turbulent Flow,** $(k - \epsilon)$ **model**, for airflow dynamics.
- **Transport of Diluted Species**, for methane dispersion.

3.4.1 Turbulent Flow (k–ϵ) Interface

The Turbulent Flow interface ($k - \epsilon$ model) is employed to solve the governing equations for incompressible turbulent airflow known as Reynolds-Averaged Navier-Stokes (RANS) equations. This approach captures the mean flow behavior while accounting for turbulent fluctuations using two additional transport equations: one for turbulent kinetic energy (k) and another for its dissipation rate (ϵ).

Since gas transport in realistic outdoor environments typically occurs under turbulent flow conditions, resolving velocity fluctuations is essential to capture dispersion realistically. The $k - \epsilon$ model is widely used in engineering simulations due to its robustness, efficiency, and suitability for general-purpose turbulent flows. It models the effects of turbulence by balancing energy production and dissipation, allowing realistic representation of turbulent behavior without resolving all fine-scale eddies, which would be computationally expensive.

The governing equations are as follows:

1. Momentum Equation - Navier-Stokes

$$\rho(\mathbf{V} \cdot \nabla)\mathbf{V} = \nabla \cdot [-pI + K] + F + \rho g \tag{3.1}$$

   This equation governs fluid motion and solves for the fluid velocity $\mathbf{V}$. The left-hand side represent the convective transport of momentum, while the right-hand side explains the forces acting on the fluid including pressure gradients combined with viscous and turbulent stresses (via the stress tensor K), external forces such as by wind, and gravity which accounts for buoyancy effects due to the density difference between methane and air.

2. k- Equation

$$\rho(\mathbf{V} \cdot \nabla)k = \nabla \cdot [(\mu + \frac{\mu_t}{\sigma_k})\nabla k] + P_k - \rho\epsilon \tag{3.2}$$

   This equation solves for turbulent kinetic energy (k), representing the intensity of turbulence in the flow. This explains how turbulence is transported, generated, and dissipated.

3. ϵ- Equation

$$\rho(\mathbf{V} \cdot \nabla)\epsilon = \nabla.[(\mu + \frac{\mu_t}{\sigma_\epsilon})\nabla\epsilon] + C_{\epsilon 1}\frac{\epsilon}{k}P_k - C_{\epsilon 2}\rho\frac{\epsilon^2}{k} \tag{3.3}$$

This equation solves for turbulent dissipation rate ϵ which determines how quickly turbulence decays over time, improving stability and accuracy of the flow field predictions.

By solving both k and ϵ equations, the model estimates μ_t, turbulent viscosity, which is used to adjust the momentum equation through K, by replacing molecular viscosity with the effective viscosity that includes turbulence effects.

$$\mu_t = \rho C_\mu \frac{k^2}{\epsilon} \tag{3.4}$$

The effective stress tensor K becomes:

$$K = (\mu + \mu_t)(\nabla\mathbf{V} + (\nabla\mathbf{V})^T) \tag{3.5}$$

Incompressibility Assumption As discussed in equation 2.24, the continuity equation for incompressible steady flows simplifies to $\nabla \cdot \mathbf{V} = 0$. This ensures that mass is conserved and there is no artificial accumulation or loss in the flow. Although air is naturally compressible, it can be treated as incompressible when the flow Mach number is sufficiently low (typically Mach number less than 0.3), meaning density variations are negligible. In this study, the characteristic flow velocities are well below this limit, so density changes have an insignificant effect on the results. Since the air is treated as incompressible in this study, this equation is inherently satisfied when solving the Navier–Stokes equations.

3.4.2 Transport of Diluted Species

The Transport of Diluted Species (TDS) interface is used to simulate methane dispersion in air. It accounts for both convective transport driven by the velocity field and molecular diffusion due to concentration gradients. This makes it well-suited for dispersion modeling, where tracking the spatial and temporal evolution of a trace gas is essential. Methane transport is governed by the convection–diffusion equation, which captures the combined effects of advection and diffusion.

1. Mass Transport Equation

   $$\nabla \cdot \mathbf{J}_i + \mathbf{V} \cdot \nabla C_i = 0 \tag{3.6}$$

   This equation ensures mass conservation of the species in the system. The two transport mechanisms are: **Diffusion** (first term) which shows the natural spread of methane molecules from regions of high concentrations to low concentrations, and **Convection** (second term), which contributes to methane being carried by airflow.

2. Fick's law of Diffusion:

   $$J_i = -D_i \nabla C_i \tag{3.7}$$

   where D_i is the diffusion coefficient of methane in the air, C_i is methane concentration.

The density and viscosity values defined in the Materials section are directly used in the Turbulent Flow interface to solve the RANS equations. Similarly, the diffusivity of methane in air is used in the TDS interface to evaluate the diffusion term.

3.4.3 Physics Coupling

These two physics interfaces are coupled within COMSOL to ensure that methane transport is governed by realistic flow dynamics of methane dispersion process in the air. The velocity field computed from Turbulent Flow $k - \epsilon$ model, is passed to the species transport equations in the TDS module. Figure 3.3 illustrates this coupling framework.

This coupling enables the simulation to account for how turbulence and wind-driven flow patterns influence methane movement and mixing. Together, these interfaces provide a consistent and physically accurate framework for analyzing methane leak dispersion under various operating conditions.

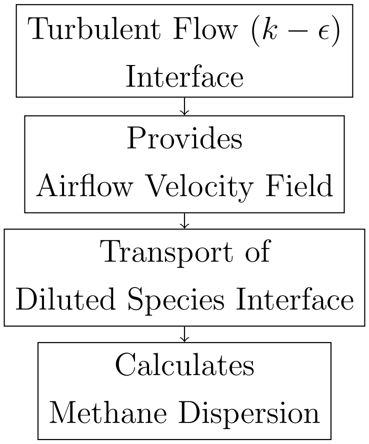

Figure 3.3: Coupling of Turbulent Flow and Transport of Diluted Species Interfaces Process

3.5 Boundary Conditions

Boundary conditions define how the simulation domain interacts with its surroundings and are critical for obtaining physically meaningful and accurate results. In this study, the boundary conditions are carefully assigned for both the Turbulent Flow (TF) and the Transport of Diluted Species (TDS) interfaces to simulate methane dispersion in an open environment.

As illustrated in Figure 3.2, the geometry includes a pipe leak as the methane source, surrounded by open boundaries that represent atmospheric surroundings. Accordingly, boundary conditions are seperately defined for the Turbulent flow and Transport of Diluted Species interfaces as follows:

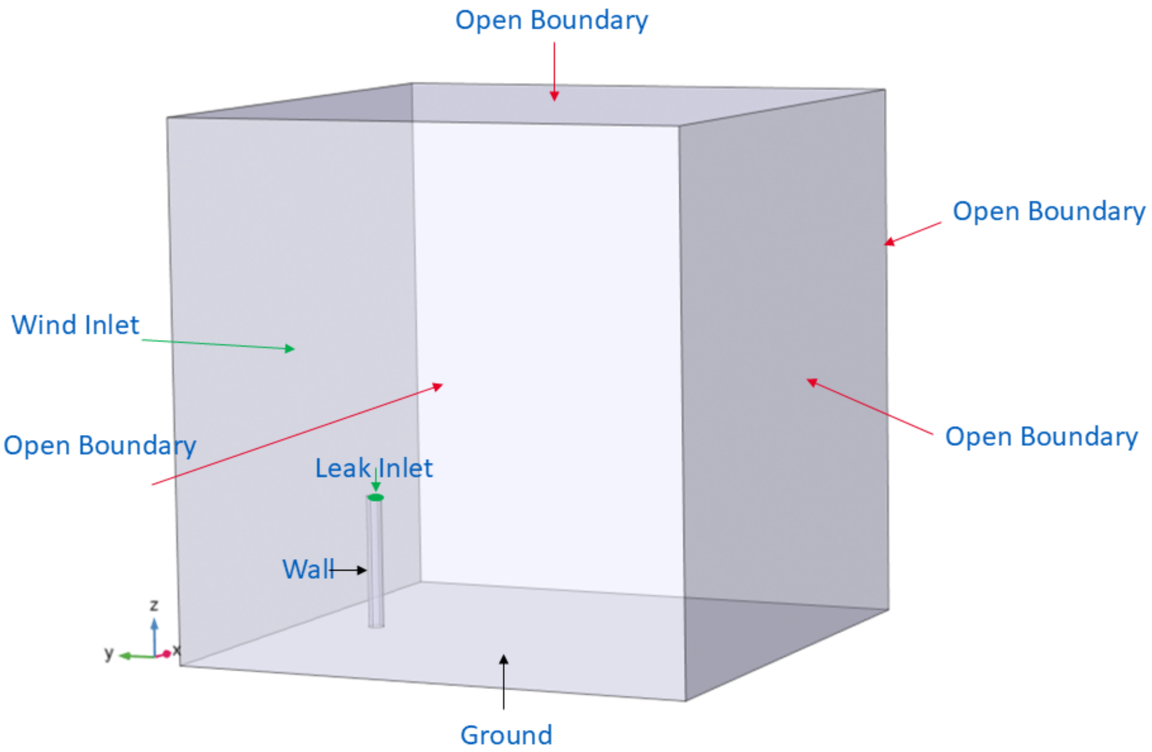

Figure 3.4: Assigned boundary conditions for the 3D simulation domain.

Boundary Condition for Turbulent Flow ($k - \epsilon$) interfaces:

- A velocity inlet is assigned at the upstream boundary to model ambient wind entering the domain in the $-y$ direction, with a wind speed v_w in m/s.
- A mass flow rate inlet condition is applied at the leak source location, which represents methane being released into the domain with a leak rate $\dot{m}$ in kg/s.
- The top and other lateral faces of domain are considered as open boundaries, with a zero normal stress condition, enabling natural flow without artificial reflection to allow fluid to exit or enter the domain freely.
- The ground and pipe walls are defined as no-slip boundaries, enforcing zero velocity to model realistic interaction with solid boundaries and to prevent non-physical inflow or outflow.

  These conditions ensure that the Navier-Stokes and turbulence model equations are solved with physically appropriate flow constraints, reflecting realistic interactions between airflow and obstructions.

Boundary Conditions for the Transport of Diluted Species Interface:

- A concentration inlet condition is applied at the methane leak source to introduce a specified methane concentration $c_{0,c}$ into the domain.
- The top and lateral side boundaries are considered as open boundaries, meaning zero external concentration, simulating atmospheric dilution.
- The ground and pipe walls ar treated as no-flux boundaries, which means there is no mass transfer of species across these surfaces, ensuring that methane does not diffuse through solid boundaries.

Figure 3.4 illustrates the boundary assignments over the 3D domain. These settings ensure methane transport is driven by both the velocity field and diffusion, consistent with environmental dispersion behavior.

Together, these carefully defined boundary conditions ensure a well-posed numerical problem. They are essential for accurately solving the governing equations discussed earlier, and for realistically simulating methane dispersion driven by wind and leak dynamics in an open realistic environment.

3.6 Mesh Strategy

After defining the physical models and boundary conditions, the next step is to build a proper mesh. Meshing refers to the discretization of the computational domain, which is necessary for solving the governing equations numerically. The precision and reliability of the results significantly depend on the quality and resolution of the mesh.

COMSOL Multiphysics uses unstructured meshing techniques, with triangular elements in 2D domains and tetrahedral or hexahedral elements in 3D simulations. Unstructured meshes are particularly useful near walls, corners, and geometrically complex regions where finer resolution is needed to capture sharp gradients in velocity, pressure, or concentration, while maintaining computational efficiency. In this study, such gradients arise near the methane jet and its interaction with the surrounding air.

COMSOL offers both physics-controlled meshing and manual refinement by the user. For this research,physics-controlled meshing was initially used, with mesh sizes (coarse, normal, fine) varied based on leak rates and wind conditions. Finer mesh was needed for certain cases to resolve steep gradients and achieve more accurate results.

Although increasing physics-controlled mesh density might greatly help to enhance numerical accuracy, it also leads to higher computational costs and longer simulation times. The challenge, therefore, was to determine an optimal mesh resolution to ensure fine resolution exists in critical areas including near the source while avoiding excessive elements elsewhere. To achieve this balance between resolution and efficiency, manual mesh refinement was applied where gradients were strongest, while less finer settings were retained elsewhere in the domain. This selective refinement strategy allowed key physical phenomena to be captured without excessive computational burden. COMSOL's built-in meshing tools and adaptive control features enabled the efficient tuning of mesh resolution based on scenario requirements.

Figure 3.5 presents a comparison between a fine and extremely coarse mesh used for the 3D geometry, along with element statistics.

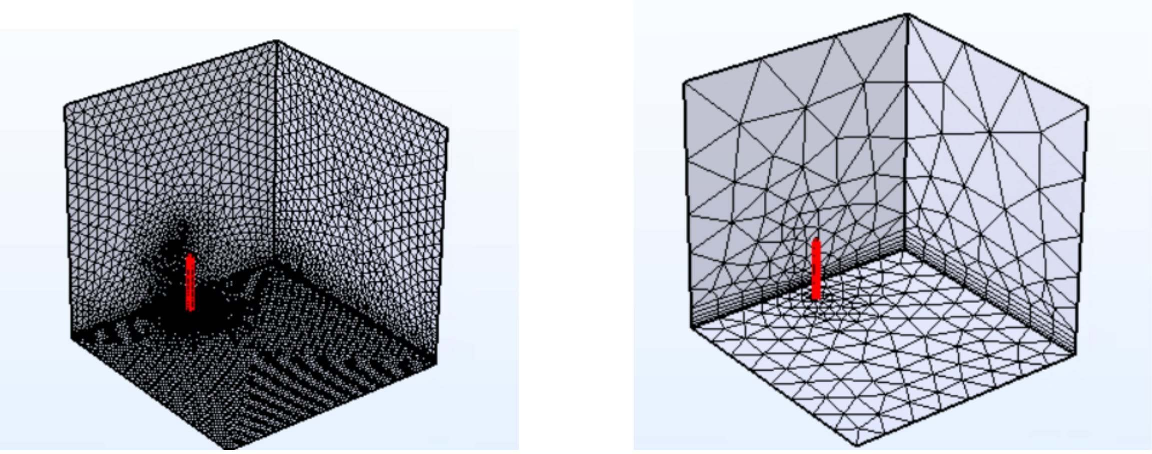

(a) Fine mesh: Mesh consists of 603440 domain elements, 19245 boundary elements, and 761 edge elements

(b) Coarse mesh: Mesh consists of 4169 domain elements, 818 boundary elements, and 124 edge elements

Figure 3.5: Comparison of mesh resolution for the 3D simulation domain.

This highlights how mesh refinement directly affects element count and the potential for capturing detailed flow features.

3.7 Solver Strategy and Study Types

After generating the mesh, the next step was to choose an appropriate study type and solver strategy to simulate methane leak behavior and observe the resulting plume dynamics. The COMSOL solver configuration in this work primarily relied on the default solver settings, which use the PARDISO linear direct solver for most physics. This solver is well-suited for handling the large, sparse systems of equations typical in CFD simulations.

3.7.1 Time-Dependent and Stationary Studies

Two study types were used in this work: a time-dependent study to capture the transient evolution of the methane plume, and a stationary study to analyze steady-state dispersion behavior.

The time-dependent study was used to resolve and monitor the early dynamics of the leak, including initial jet formation, turbulent mixing, and early spread of methane into ambient air. A carefully selected time step was applied to ensure both numerical stability and adequate resolution of transient features.

Once transient effects were observed, the simulation was transitioned - *when applicable* [1]- to a stationary study . This allowed the analysis to focus on the steady-state behavior of the plume, where transient effects had diminished and the flow field had reached a stable regime.

The primary goal of using a stationary study was to examine the fully developed flow field under steady wind, where the plume exhibits smooth, continuous flow without recirculation, trapping, or excessive turbulence. This approach enabled accurate analysis of the resulting concentration profiles for leak rate estimation in image-based quantification approach (explained in next chapter), while avoiding the computational cost of extending the transient simulation unnecessarily.

---

[1] *When applicable* refers to simulation scenarios where the plume behavior reaches a quasi-steady state after an initial transient period, allowing the use of a stationary solver to analyze long-term dispersion. However, in cases involving persistent unsteady behavior, such as high turbulence, the stationary solver may fail to converge

3.8 Post-Processing

3.8.1 Result Visualization and Data Extraction

Following the completion of the simulation study, post-processing was carried out using COMSOL's integrated visualization tools to interpret the results both qualitatively and quantitatively. The Results module offers a variety of plot types and data extraction features to evaluate flow behavior, velocity and concentration distribution, pressure gradients, etc.

Key post-processing tools used include:

- **Contour Plots**: Used to display variations in velocity, pressure, or concentration within the computational domain
- **Streamline Plots** : Used to track the direction and structure of fluid flow, providing insight into the transport pathways of the methane leak under different wind conditions.
- **Cross-Sectional slices**: Applied at selected planes to examine flow properties such as velocity and concentration at specific depths or regions of interest.
- **Derived Values**: Used to extract numerical data from specific points, lines, surfaces, and subdomains within the model. These values include maximum velocity, and mass flux, providing a quantitative foundation for further analysis
- **Tables and Reports**: In addition to visual analysis, quantitative data such as methane concentration fields were exported in tables for further processing. This enabled the creation of custom images and detailed quantification of leak behavior, as described in the next chapter.

3.9 Model Assumptions Summary

To simplify the simulation setup and maintain computational feasibility, the following assumptions were considered:

- Air is treated as incompressible gas.
- Ambient temperature is constant at 25 °C; thermal effects on buoyancy are neglected.

- No chemical reactions occur between methane and air.
- Wind is steady and uniform across the inlet face.
- The domain boundaries do not introduce artificial reflection or confinement effects.

These assumptions allow the model to focus on the primary dispersion characteristics of methane under varying leak rates and wind conditions.

Chapter 4

Image-Based Quantification Methodology Using CFD Data

4.1 Framework Overview

This chapter presents an image-based post-processing framework designed to transform CFD simulation results into meaningful insights for methane leak quantification. Following the physics-based simulations, a structured workflow was implemented in MATLAB to interpret the resulting concentration fields and facilitate systematic interrogation of plume behavior as it would appear to a real-world sensing system.

The post-processing procedure consists of three key stages: verification, projection, and quantification.

Verification To verify the accuracy of data interpretation during post-processing, concentration fields were reconstructed and visually compared to the original simulation outputs, ensuring numerical consistency and reliable data handling. Details of this process are presented in Section 4.2.

Projection converts the 3D concentration data into 2D images, replicating how gas imaging systems would capture these gas leaks in real-world applications. These systems do not observe full volumetric data but instead detect line-of-sight integrated concentrations, as discussed in Section 2.1. Because gases such as methane are transparent in the visible spectrum, the optical signal depends on the total amount of gas along the sensor's viewing path, which is obtained by integrating the concentration in that direction.

Quantification is then performed using a custom MATLAB algorithm based on the principle of mass conservation, as explained in Section 2.4.6 . By analyzing the (2D) projected concentration fields, this algorithm estimates the methane leak mass flow rate. This enables the simulation output to be translated into actionable environmental metrics, which is essential for greenhouse gas emission monitoring and leak detection systems.

4.1.1 Importing and Structuring Simulation Data

Although the overall procedure is part of post-processing, the initial steps including importing, organizing, and preparing the data for visualization are referred to as pre-processing in this context. The exported methane concentration field from simulated results were imported into MATLAB as CSV files, each containing spatial coordinates (x, y, z) and the corresponding concentration values.Once imported, the data was organized into structured arrays and interpolated onto a regular grid, which enabled further visualization and numerical analysis.

This interpolation step is essential for downstream operations such as projection along a viewing axis to obtain line-of-sight integrated concentrations. It is worth noting that while finer grids provide a more accurate reconstructions, they may also increase memory requirements and computational time. Therefore, grid resolution was adjusted based on the desired trade-off between accuracy and efficiency.

A simple correction was also applied to eliminate any small negative concentrations introduced during simulation and/or interpolation. No filtering or smoothing was necessary, as the data originated from a numerical simulation and were free from noise. Normalization was also not applied in this study, but is noted as a useful pre-processing option when comparing multiple datasets. However, such steps would be required when handling real experimental or field data.

Key preprocessing steps included: Reading and parsing CSV files, reformatting scattered data into structured 2D or 3D grids (based on CFD domain) using interpolation, eliminating small negative concentrations introduced during simulation or interpolation, avoiding unnecessary smoothing or normalization, since the simulation data were noise-free.

Overall, these pre-processing operations ensured that the imported concentration fields remained physically consistent and were properly structured for accurate visualization, projection, and quantitative analysis.

4.2 Visualization for Verification

Visual inspection was used to validate the integrity of the imported simulation data and pre-processing. Through this image-based approach, the regenerated plots were visually compared with their corresponding simulation outputs.

For 2D cases, surface and contour plots of the methane plume were recreated in MATLAB using the exported concentration field datasets. Figures 4.1 and 4.2 show a side-by-side comparison of representative plots for two different 2D scenarios.

In figure 4.1, the case involves a high-pressure leak with ambient wind, two $20\,(\text{m}) \times 30\,(\text{m})$ obstacles. The visualization corresponds to 5 seconds post-release. Minor differences are visible in the contour smoothness and in the fine-scale eddy structures around the obstacles. These deviations arise from interpolation during data export and differences in the contouring algorithms used by MATLAB and COMSOL.

Figure 4.2 illustrates a second 2D simulation, validating the reconstruction of the plume shape and gradient distribution through surface plots. The case shown in the figure represents a low-pressure methane leak with wind blowing from left to right and without obstacles. However, there are slight variations in color mapping and gradient sharpness in Figures 4.2a and 4.2b , which attributes to the interpolation and therefore the image resolution.

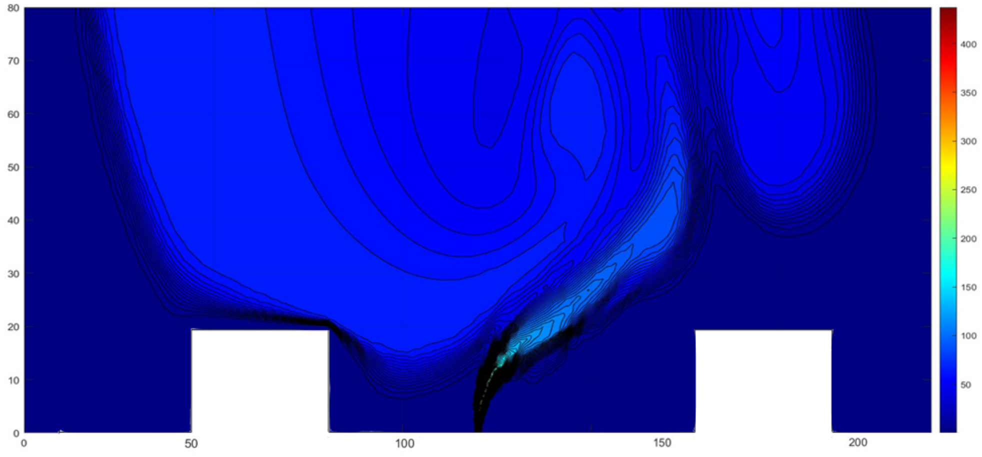

(a) Reconstructed contour plot in MATLAB from exported CFD concentration data.

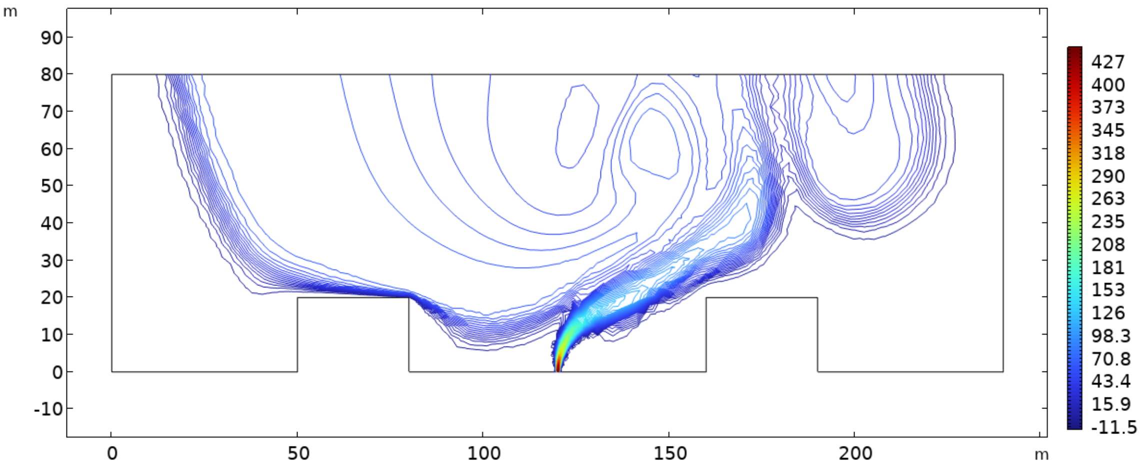

(b) Contour plot of methane concentration from the original CFD simulation.

Figure 4.1: Comparison of original CFD simulation and regenerated contour visualizations for a 2D methane leak scenario.

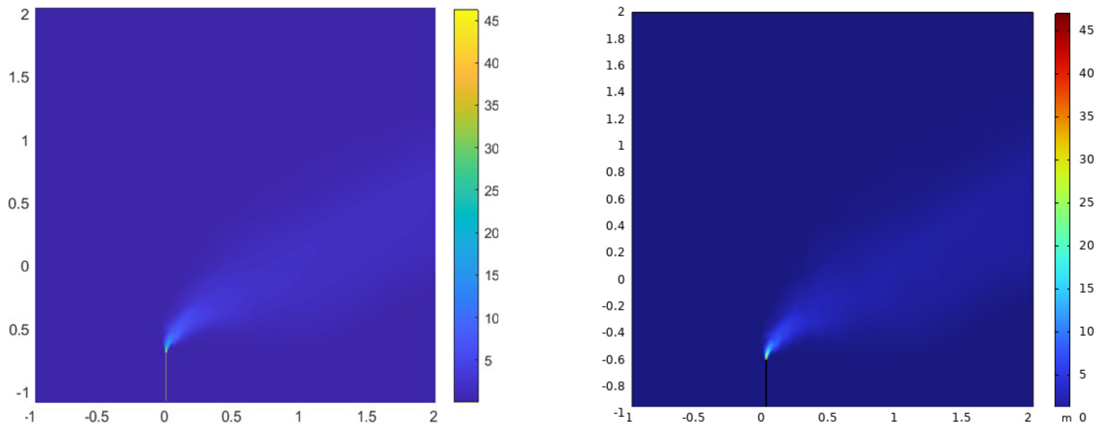

(a) Surface plot reconstructed in MATLAB from exported concentration data.

(b) Surface plot of methane concentration from the corresponding CFD simulation.

Figure 4.2: Comparison of original CFD simulation and regenerated surface visualizations for a 2D methane leak scenario.

For 3D simulations, slice plots and volumetric renderings were performed to visualize and reconstruct the methane concentration datasets and the results were consistent with the corresponding CFD outputs.

Care was taken to match visual parameters such as colormaps, axis limits, and resolution settings to ensure a fair comparison.

A close visual match between the reconstructed concentration plots generated in MATLAB and the original simulation data from CFD model confirmed that the data import, interpolation, and visualization procedures were correctly implemented. This verification was essential before proceeding to the projection and quantification steps.

4.3 Projection Methodology

To analyze how methane leaks would appear to real-world imaging and detection systems such as WMS or FMCW, the volumetric 3D concentration field generated by the CFD simulations must be projected onto a 2D plane. This projection step transforms the simulation data into a form that replicates what a sensing system would perceive during field measurements.

Since most practical gas detection technologies rely on optical line-of-sight measurements, they do not capture the full volumetric gas distribution but rather a path-integrated representation of gas concentrations along a specific viewing direction. Therefore, this projection is essential not only to generate realistic visualizations from the sensor's perspective but also to enable a reliable leak quantification algorithm.

In this framework, the image-based projection algorithm transforms the 3D gas concentration field into 2D integrated-path concentration maps on three standard orthogonal planes: XY (top-down view), YZ (side view) and XZ (front view), as illustrated in Figure 4.3. These projections simulate how a real gas sensing system would perceive the gas plume when oriented along the z-, x-, or y-axis, respectively. The selection of these planes is based on the ideal perspectives of typical gas detection setups, where sensors or cameras are placed in various positions relative to the plume.

The projection technique is performed by integrating the 3D concentration field along the axis normal to the selected viewing plane. For example, when projecting onto the YZ plane, the concentration values are integrated along the X-axis, collapsing the 3D dataset into a 2D representation as written mathematically in equation 4.1.

$$C_{proj}(y, z) = \int C(x, y, z)dx \tag{4.1}$$

Similar transformations are applied for the other planes, as shown in equations 4.2 and 4.3, to create comprehensive visualizations of the gas dispersion.

$$C_{proj}(x, y) = \int C(x, y, z)dz \tag{4.2}$$

$$C_{proj}(x, z) = \int C(x, y, z)dy \tag{4.3}$$

In practice, the integration is carried out numerically over the discretized domain, consistent with the structure of the exported simulation data as follows:

$$C_{proj} = \sum_i C_i \Delta d \tag{4.4}$$

where Δd is the grid spacing in the d direction (i.e., the line of sight). The resulting C_{proj} are the integrated values and have units of mol/m^2, forming the quantitative basis for subsequent leak rate estimation.

The projected concentration fields are visualized in standard 2D plotting methods. Visualization parameters, such as colormap scaling and shading, were adjusted where needed to improve contrast and highlight spatial concentration gradients. These views reflect common sensor placements in field deployments and enable flexible analysis depending on sensor orientation relative to the plume.

Accurate projection is a critical step, as it directly affects the next stage, leak quantification. The resulting 2D fields serve as input data to the mass-based estimation algorithm, enabling methane leak rate to be computed based on image-derived concentration distributions.

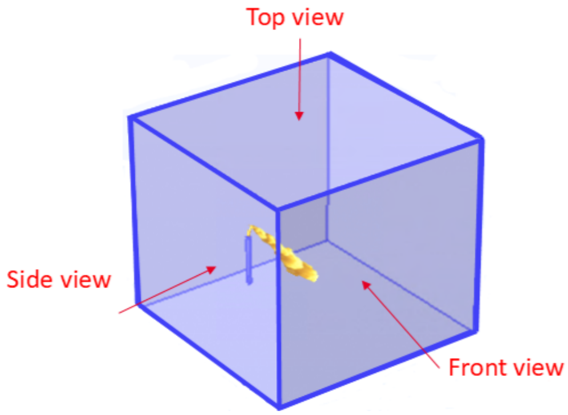

Figure 4.3: Schematic representation of the projection views.

4.4 Quantification Algorithm

With the path-integrated concentration maps obtained from the projection step, the next objective is to estimate the methane leak rate. This metric is essential for real-world methane leak detection, as it enables assessment of emission severity and informs necessary mitigation actions (see Section 1.1). In this context, quantification refers to estimating the methane leak's mass flow rate, based on the projected concentration data, using an image-based algorithm built around the principle of mass conservation.

As previously introduced in the equation 2.15 the general form of mass flux through a surface is given by:

$$\dot{m} = \int_{\mathbf{A}} \rho \mathbf{V} \cdot d\mathbf{A} \tag{4.5}$$

where ρ is the local gas density, V is the velocity vector, and dA is the differential surface area element normal to the flow direction. However, since optical detection systems and CFD outputs deal with molar concentration fields $C(x, y, z)$ (in units of

mol/m^3)instead of density, the relationship between them becomes:

$$\rho = C\,M \tag{4.6}$$

where M is the molar mass of methane. Therefore, substituting this into equation 4.5 yields, where imaginary detection system's line of sight and wind are in y direction :

$$\dot{n} = \int_A C\,\mathbf{V} \cdot \hat{\mathbf{n}}\,dA \tag{4.7}$$

Here, $\dot{n}$ is the molar flow rate in mol/s and can be converted to mass flow rate $\dot{m}\,(g/s)$ using methane molar mass M.

This quantification approach lays on the idea of computing the total flux of methane across a surface perpendicular to the plume direction, which is aligned with the y-axis. This leads to:

$$\dot{n} = \int_z \int_x C(x, y, z) v_y(x, y, z)\,dxdz \tag{4.8}$$

The velocity component v_y is perpendicular component to the selected plane, and is aligned with the wind direction, which is the main transport axis of the methane plume in this study.

4.4.1 Side view projection

In the side view analysis, the 3D concentration field was projected along the x- axis (line of sight), producing a path-integrated concentration map $C_{proj}(y, z)$ on the YZ plane:

$$C_{proj}(y, z) = \int C(x, y, z)dx \tag{4.9}$$

And assuming a uniform wind velocity v_w across the projection plane, which is a reasonable simplification under controlled steady-state plume behavior based on simulation, the velocity field simplifies to:

$$v_y(x, y, z) = v_w \tag{4.10}$$

Substituting these into the molar flow rate equation X yields:

$$\dot{n} = v_w \int C_{proj}(y, z) dz \tag{4.11}$$

This expression represents the total molar flow rate through a vertical XZ plane. In practice, this integral is approximated numerically using the discrete dataset

$$\dot{n} \approx v_y \sum_i C_{\text{proj}}(y, z_i) \Delta z \tag{4.12}$$

4.4.2 Top view projection

For top-view analysis, the concentration field is projected along the z- axis, resulting in a path-integrated concentration map $C_{proj}(x, y)$ on the XY plane

$$C_{proj}(x, y) = \int C(x, y, z) dz \tag{4.13}$$

This projection yields a top-down view of the gas plume on the XY plane. Since the wind, and thus the primary direction of plume transport, occurs along the y-axis, the molar flux can be estimated by integrating the projected concentration along the x-direction at a fixed y-location. This approach effectively evaluates the total methane transport through a cross-section perpendicular to the plume trajectory, assuming a uniform velocity field, as expressed by:

$$\dot{n} = v_y \int C_{proj}(x, y) dx \tag{4.14}$$

Numerically in discrete form:

$$\dot{n} \approx v_y \sum_j C_{\text{proj}}(x_j, y) \Delta x \tag{4.15}$$

This method is similarly valid, provided that the cross-section is sufficiently far from the source such that the plume is fully developed. It offers a complementary way to estimate the same quantity from a different projection perspective.

4.4.3 Front view projection

While front view projection produces a visual representation of the plume on the XZ plane, the resulting 2D image lacks any information about the transport direction (e.g. y direction), since it has been integrated out. As such, this view is useful for visualization but excluded from leak rate estimation.

Once the molar flow rate $\dot{n}$ is obtained from the side or top projection, the final step is to convert it into mass flow rate. as follows:

$$\dot{m} = \dot{n} \cdot M \tag{4.16}$$

This approach preserves the physical foundation of mass conservation while adapting it to the discretized structure of the simulated data. By integrating path-concentration and assuming known wind conditions, it yields the methane leak rate in grams per second, a practical and interpretable metric. Overall, this method provides an efficient, scientifically grounded framework for quantifying emissions from simulated dataset under realistic flow conditions.

4.4.4 Selection of Quantification Plane Location

In both the side view (YZ projection) and the top view (XY projection) quantification approaches, the integration is performed over the XZ plane located at a fixed y-position, perpendicular to the transport direction. For reliable mass flow rate estimation, this location must be sufficiently far downstream of the leak source, where the methane plume has fully developed and reached a quasi-steady state.

While the term “sufficiently far” is often used qualitatively, in this study it is treated quantitatively: the optimal location was also determined by identifying the point beyond which both the plume shape and the estimated mass flow rate ($\dot{m}$) changes were negligible with further downstream movement (see Section 5.6 for corresponding results). If the projection is taken too close to the source, it may capture the transient jet region or early mixing, leading to underestimation or variability in the calculated mass flow rate.

The optimum downstream location varied between cases, depending on parameters such as wind velocity, leak rate, and domain setup. A dedicated analysis of this convergence behavior, including an error versus distance plot, is provided in Chapter 5. This careful and quantitative placement of the observation location ensures that the computed leak rate represents the true steady-state behavior of the plume rather than the early-stage dynamics.

Chapter 5

Results and Discussion

This chapter presents and discusses the results of the methane leak dispersion simulations and the subsequent image-based quantification framework. It begins with a qualitative validation of the simulation model through comparison with an established reference study to assess physical accuracy and realism. This is followed by a series of 2D visualizations that reveal the plume behavior under varying environmental and release conditions. The discussion highlights key flow and dispersion characteristics, emphasizing their relevance to leak detection scenarios. In later sections, image-based datasets are generated using line-of-sight projection, and the methane emission rates are estimated and analyzed using the proposed quantification approach. The results are interpreted to evaluate the accuracy, limitations, and practical implications of the framework.

5.1 Visual Validation Against Literature

While numerical modeling offers detailed insights into gas dispersion, its reliability must be confirmed by comparing results with experimental data or established literature. A well-calibrated and validated model not only improves our understanding of gas dispersion but also strengthens confidence in simulated outcomes and supports its application in methane monitoring and mitigation frameworks.

To verify the physics setup and CFD modeling approach used in COMSOL Multiphysics, initial benchmark cases were designed to replicate scenarios reported in a reference study [36]. In these benchmark simulations, the methane plume structure is observed under different wind conditions. Methane is modeled as a light gas dispersing in air, influenced by buoyancy, turbulence, and environmental flow.

The reference case is modeled in a 2D computational domain measuring 240 m width and 80 m in height. Two rectangular buildings, each 30 m wide and 20 m high, are positioned on the ground. The inclusion of buildings in the domain adds realistic flow separation that mimics realistic urban environments and influences how gas plumes behave in such settings. A circular emission hole (20 cm in diameter) is located at ground level between the two buildings.

In methane release scenarios, this circular point serves as the source, modeled at a high pressure of 11 bar to simulate industrial pipeline leak conditions, consistent with the reference setup [36]. Also, two wind conditions with velocities at 0 and 10 m/s were considered. These dimensions and conditions were adopted from the reference study [36] to enable direct visual and physical comparison.

5.1.1 Wind-Only Case (No Methane Release)

The first simulation considers wind-only flow, with no methane present, to establish a baseline understanding of airflow dynamics within the domain. This allows for clear identification of key flow features, particularly how wind interacts with obstacles, and the resulting recirculation zones.

Wind enters from the left boundary at a velocity of 10 m/s, flowing toward the right. The buildings and ground are treated as no-slip wall conditions, while the top and outlet boundaries are defined as open with zero pressure. The simulation is solved under steady-state conditions.

The resulting velocity field is shown in Figure 5.1a, which reveals a large recirculation region between the two buildings. This closely matches the behavior reported in the reference study, illustrated in Figure 5.1b. The agreement confirms that the implemented boundary conditions, physics models, and solver settings accurately capture urban wind flow dynamics. This steady wind field is later used as the initial condition for subsequent simulations involving methane release.

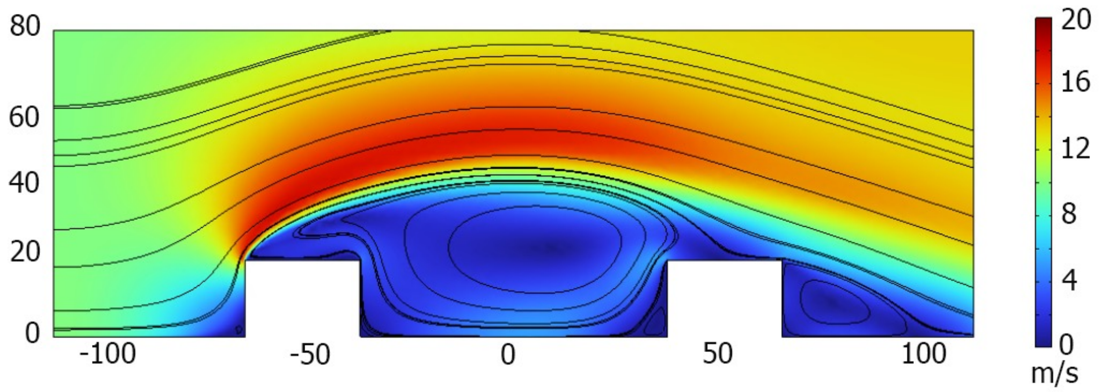

(a) Present simulation result showing streamlines of wind flow over urban obstacles at 10 m/s.

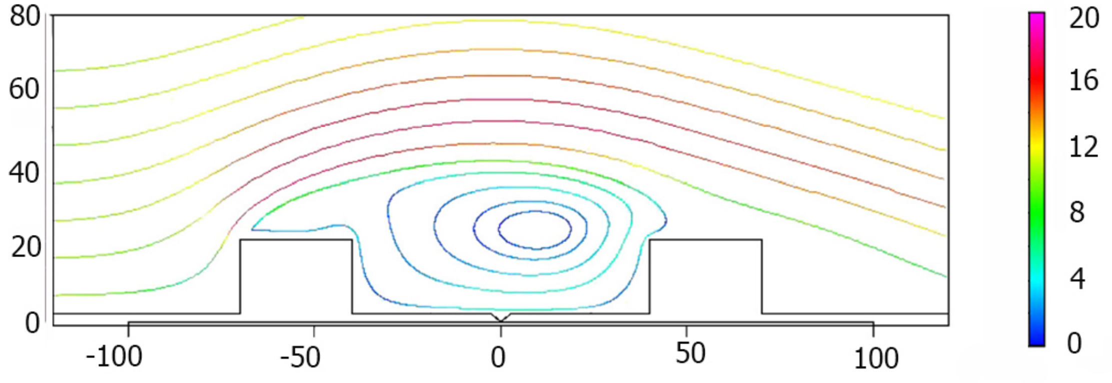

(b) Reference study result adapted from [36], showing similar recirculation zones ,flow patterns and velocity range.

Figure 5.1: Streamline comparison of steady wind flow at 10 m/s over two rectangular buildings. The present simulation closely replicates the flow structure reported in the reference, validating the CFD setup.

5.1.2 Methane Release

In this case, methane is released from a 20 cm-wide circular hole on the ground at a high pressure of 11 bar. Due to the significant pressure difference between the source and ambient conditions (1atm), a high-velocity jet is formed, exhibiting characteristics of a compressible flow. The maximum velocity reaches approximately 438 m/s,which is relatively close to the 420 m/s reported in the reference study[36], approaching sonic speed at the nozzle exit.

As shown in Figure 5.2a, the simulated velocity field streamlines one second after methane is released into the air. The resulting plume rises nearly 60 meters vertically, forming a narrow high-speed jet. On the left and right sides of the plume, two recirculation zones are observed, which arise from the interaction of jet momentum, turbulent mixing, and the surrounding wind effects. These features capture the core jet structure, its vertical development, and asymmetry driven by environmental flow conditions.

For comparison, Figure 5.2b shows a similar release scenario from the reference study [36], where velocity streamlines illustrate comparable jet behavior and recirculation dynamics. The strong agreement between the present simulation and prior literature reinforces the physical validity of the model and its ability to replicate key phenomena associated with methane dispersion in complex environments.

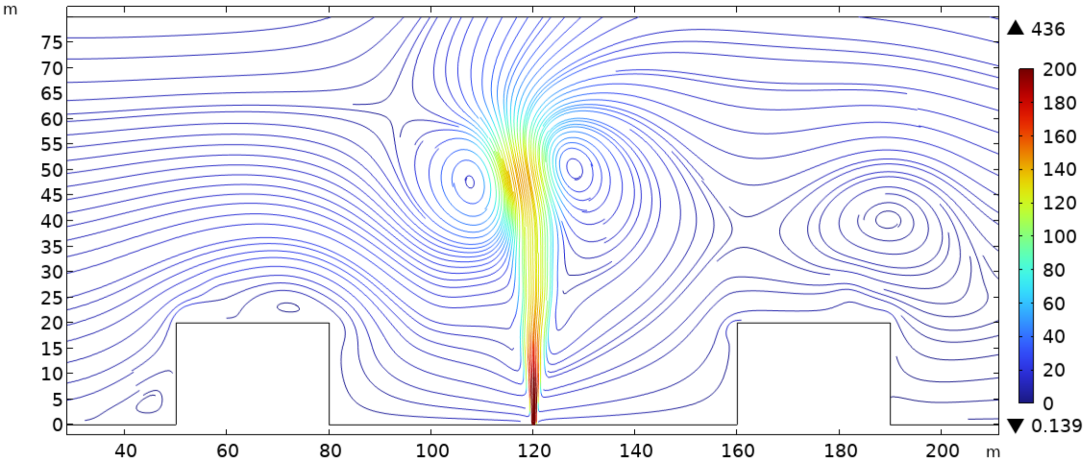

(a) Present simulation showing vertical jet structure and associated recirculation zones.

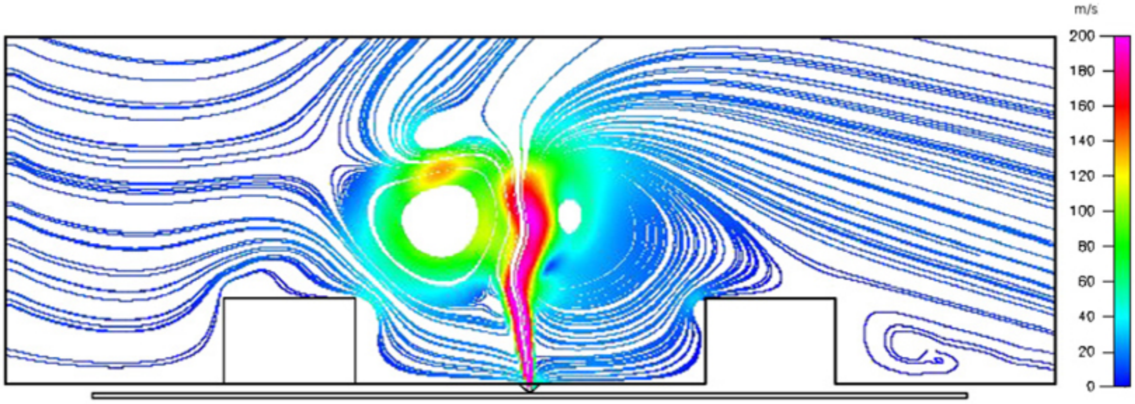

(b) Reference study [36] showing similar jet structure and vortex formation.

Figure 5.2: Comparison of methane jet velocity fields 1 second after release.

To investigate the plume development under continued release conditions, Figure 5.3 presents a comparison of velocity and concentration fields 7.5 seconds after methane release.

The results demonstrate that the methane dispersion, shown in Figure 5.3b is strongly governed by the underlying velocity field in the domain shown in Figure 5.3a. Since the Transport of Diluted Species interface rely on the velocity data provided by the turbulence model, the resulting concentration plume closely follows the flow streamlines. This is evident in the overall direction and spread of the methane plume, which indicates that the two fields are functionally coupled.

It is noteworthy that despite their visual similarity, the velocity and concentration fields describe fundamentally different physical phenomena. The velocity field reflects how air and gas move dynamically through the domain, while the concentration field shows the spatial distribution of methane due to convection and diffusion. These differences are particularly relevant for leak detection and quantification, which are based on accurate concentration mapping.

The high initial momentum of the methane jet causes it to rise vertically, but over time, the influence of wind and buoyancy overtakes the jet's upward force. This transition can be seen clearly in all simulations shown in Figure 5.3. The overall behavior remains consistent with previous CFD study shown in Figure 5.3c, which captures key dispersion features and validates the physical realism of the model.

The discrepancy arises from differences in how turbulence is treated in two-dimensional versus three-dimensional simulations. In the reference study, Large Eddy Simulation (LES) model was applied using CFD-ACE+, which resolves large turbulent structures directly and requires full spatial variation in all three directions to be physically meaningful. In 2D, the absence of spanwise variation makes such structures unrealistic or entirely absent.

While CFD-ACE+ permits LES in 2D, this is not physically rigorous. Instead, it may be used to explore qualitative trends rather than resolve detailed turbulence features. COMSOL, by contrast, disables LES in 2D, since the method is fundamentally intended for 3D turbulence and relies on dynamics, such as spanwise eddies, that are absent in two dimensions.

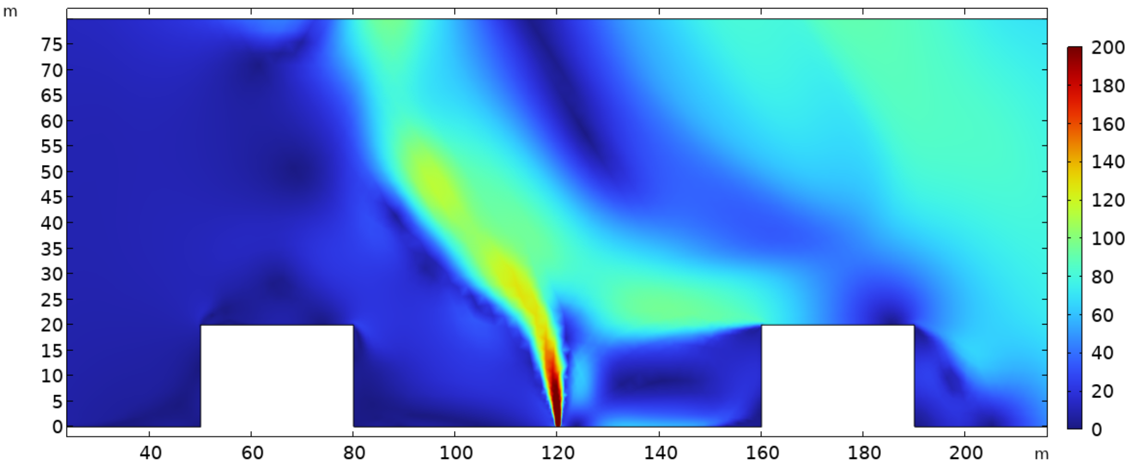

(a) Velocity magnitude in the present study.

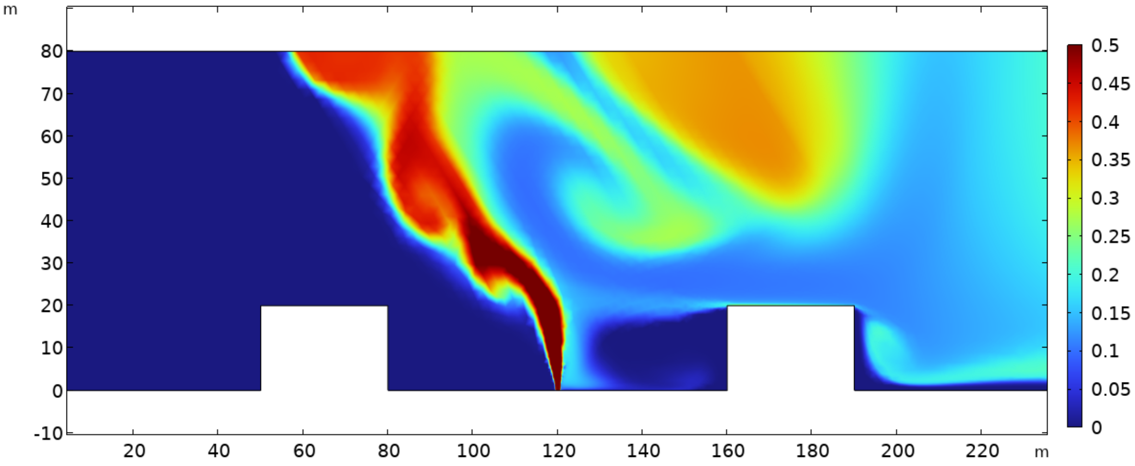

(b) Corresponding methane concentration field in the present study.

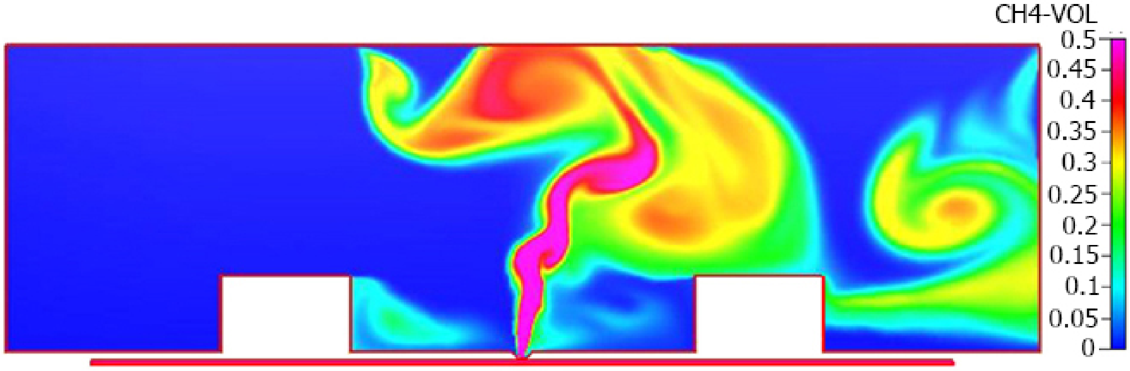

(c) Reference study concentration field.

Figure 5.3: Comparison of methane leak simulation results at 7.5 seconds after release.

5.2 Main CFD Simulation Framework and Plume Behavior

With the model's physical accuracy established through comparison with a published study, the focus now turns to the main simulation framework developed in this research. These simulations are designed to capture realistic, small-scale methane leaks, originates from a circular pipeline orifice, in a three-dimensional open-air domain under controlled ambient conditions.

The goal is first, to analyze how key parameters influence low-pressure methane leak dispersion; and second, to produce realistic, path-integrated concentration datasets that simulate what optical detection systems would perceive. These outputs are then used in the quantification process to estimate the methane leak rates.

By focusing on this underrepresented regime of small-scale methane emissions, the study aligns with current priorities in environmental monitoring [11]. Unlike highly transient large-scale events, smaller leaks tend to reach stable dispersion patterns, allowing for more accurate and computationally efficient simulation. This shift is critical for enabling early quantification and supporting actionable methane mitigation strategies.

5.2.1 3D Visualization of Methane Plumes

To understand the overall shape and spread of the methane plume in three dimensions, volumetric isosurface plots are generated for two environmental conditions: with and without wind. Figure 5.4 illustrates these cases for a 3 cm-radius leak releasing methane at 10 m/s. Figure 5.4a shows the result in a no-wind environment, while Figure 5.4b corresponds to the case with a 5 m/s wind applied from left to right. These volumetric visualizations provide an intuitive spatial impression of how the gas disperses in open air under external influence.

As expected, the presence or absence of wind produces markedly different plume shapes. In the wind-driven case, the plume is clearly transported in the downwind direction, while without wind blowing in the domain, the plume continues to evolve and rise due to buoyancy. This contrast emphasizes the importance of environmental influence on simulation strategy.

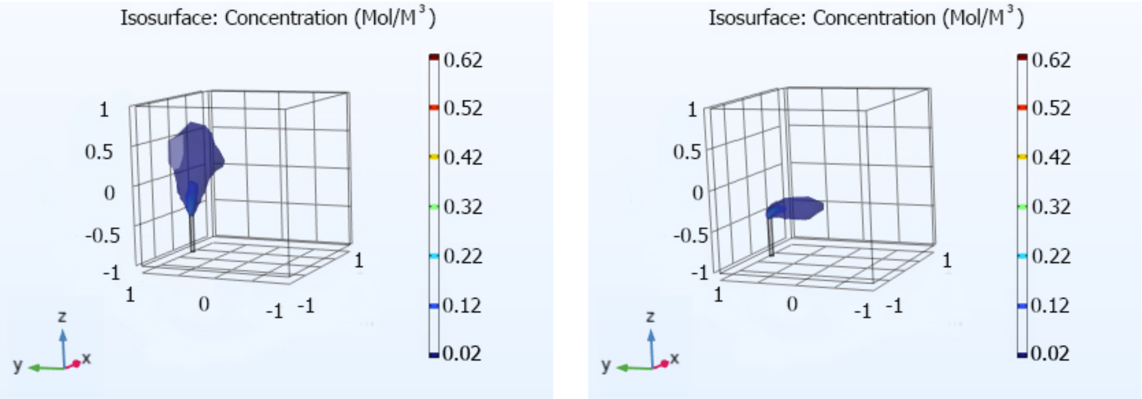

(a) No-wind case at $t = 1$ s: the methane plume expands vertically under buoyancy.

(b) Wind at 5 m/s: the plume is displaced downwind and reaches a steady-state shape.

Figure 5.4: Volumetric isosurface plots of methane concentration for a 3 cm-radius leak at 10 m/s, under different wind conditions.

To further illustrate the 3D spatial dispersion of methane, horizontal slice plots at two different elavations are presented in Figure 5.5. These slices are extracted perpendicular to the initial leak direction, and parallel to the wind flow (x-direction), at two heights: the release height (at z = 0 m) and a higher cross-section (at z = 0.4 m). Together, these layered visualizations offer insight into how the concentration field evolves with height and distance from the source within the 3D domain.

At z = 0, the concentration is strongest near the source, forming a compact, dense region around the release point. In contrast, the z = 0.4 m slice shows a more diluted and stretched concentration pattern, which indicates that the plume has risen and stretched downwind due to buoyancy and wind advection.

The slice plots help capture how concentration varies across different horizontal or vertical layers, highlighting the combined effects of wind advection, buoyancy-induced rise, and molecular diffusion, all of which shape the lateral and vertical spread of the plume structure. This analysis supports a more complete understanding of the spatial structure of the plume in open-air leak scenarios.

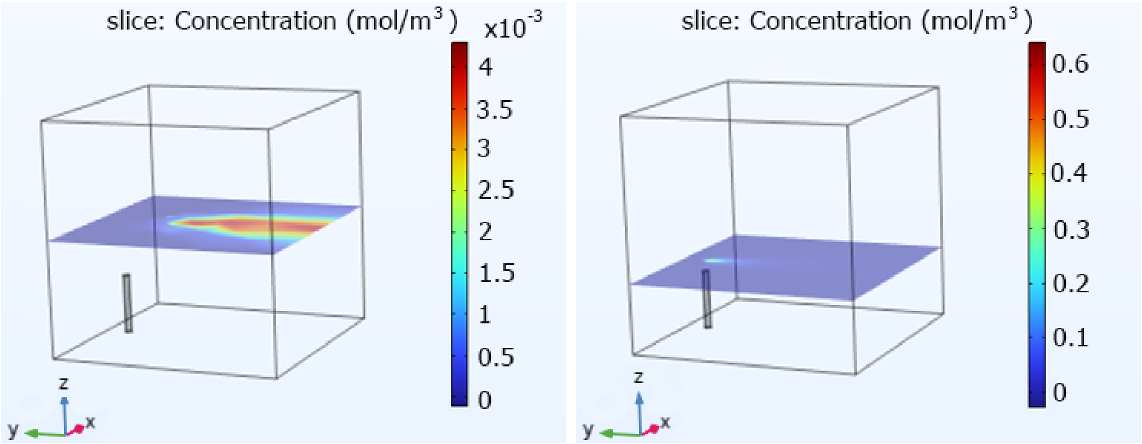

(a) Methane concentration slice at $z = 0m$. (b) Methane concentration slice at z = 0.4 m.

Figure 5.5: Horizontal slice plots of methane concentration under 5 m/s wind (in -y direction) at two elevations.

5.2.2 Temporal Evolution of the Plume

To understand how the methane plume evolves over time, a time-dependent analysis was performed using transient simulations. Figure 5.6 illustrates this development through a sequence of side-view slices at three representative time steps (e.g., 0.002 s, 0.02 s, and 0.2 s). In this scenario, the wind is blowing in -y direction at 5 m/s and leak velocity is 50 m/s, resulting in methane being generated at the rate of 0.085 kg/s. These frames capture the early evolution of the plume as it interacts with ambient wind.

At the earliest moment (0.002 s), the leak initiates as a compact vertical jet directly above the source. By 0.02 s, the plume begins to tilt and spread downwind, indicating that ambient wind becomes the dominant transport mechanism within fractions of a second. At 0.2 s and later, the plume shows a well-developed shape aligned with the wind direction, confirming that the leak reaches a quasi-steady dispersion state within a short time.

In contrast to the high-momentum jets examined during validation in section 5.1.2, these findings demonstrate behavior more representative of low-rate ambient leaks, where wind and buoyancy effects quickly surpass inertial momentum. These results underscore the importance of environmental forcing in shaping the dispersion dynamics of leaks.

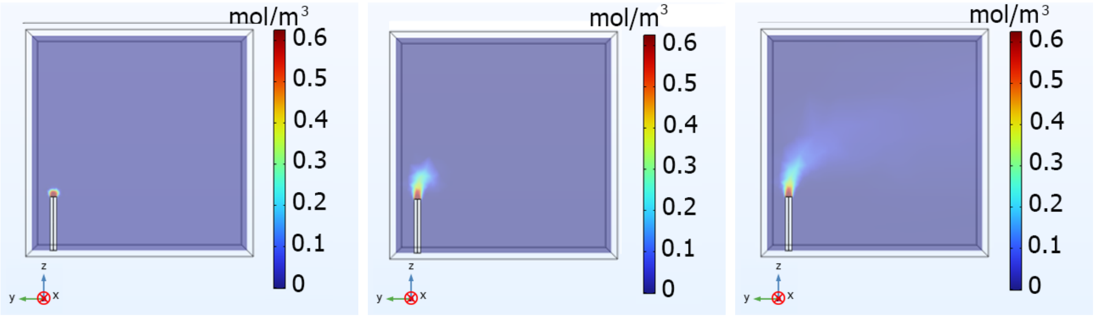

(a) Methane concentration field at t= 0.002 (s)

(b) Methane concentration field at t= 0.02 (s)

(c) Methane concentration field at t= 0.2 (s)

Figure 5.6: Time evolution of methane concentration vertical slices (side view) at source location at different times after release. Wind speed = 5 m/s, Leak speed = 50 m/s.

5.2.3 Parametric Studies: Influnce of Wind and Leak Velocity

To better understand the dynamics of methane dispersion under varying environmental and release conditions, a set of parametric simulations was performed. In particular, this section examines how wind speed and leak velocity individually affect the plume's shape, trajectory, and behavior, while keeping the leak velocity constant at 5 m/s.

To evaluate how different wind velocity conditions affect the transport behavior of methane, simulations were carried out at three different wind speeds at 0.5 m/s, 2 m/s, and 10 m/s to represent calm, moderate, and strong wind scenarios, respectively. Figure 5.7 presents the velocity magnitude fields with superimposed streamlines in side view to show how the gas flows under each wind condition.

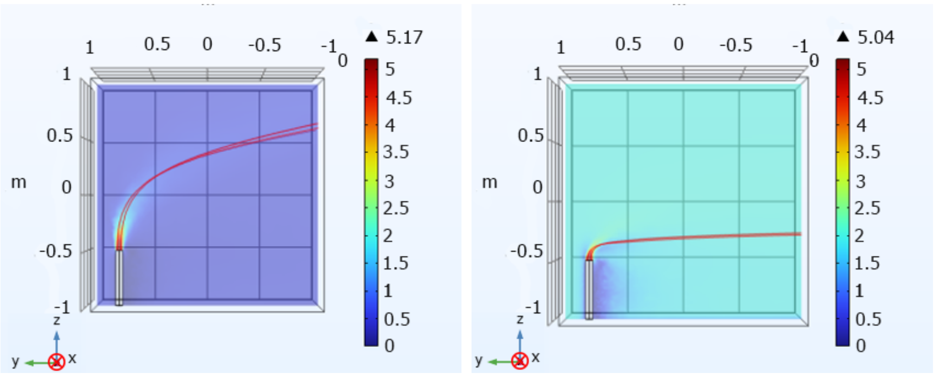

(a) Low wind (0.5 m/s) allows buoyancy to dominate, leading to a primarily vertical rise.

(b) Moderate wind (2 m/s) increases plume bending while still preserving some vertical rise near the source.

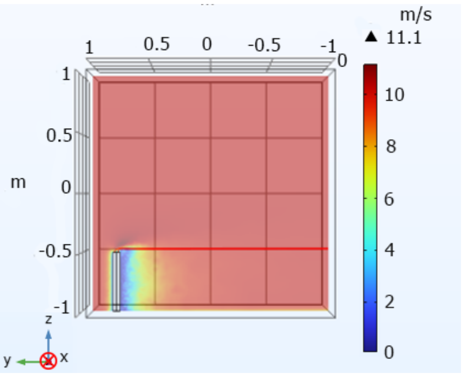

(c) High wind (10 m/s) suppresses vertical rise, resulting in a fully deflected horizontal plume.

Figure 5.7: Side-view velocity magnitude slices with streamlines showing the effect of different wind speeds on a methane leak with constant inlet velocity of 5 m/s.

As shown, relatively low wind speeds such as 0.5 m/s (Figure 5.7a) results in a plume that rises more vertically dominated by buoyancy forces rather than advection. As the wind speed increases (Figure 5.7b), the plume begins to bend in the wind direction, with more horizontal transport, as expected. Under high wind conditions (Figure 5.7c), the plume is carried almost entirely downstream following the wind path, forming a flattened downstream profile.

These comparisons underscore the importance of wind speed in shaping plume behavior. The transition from buoyancy-dominated to wind-dominated regimes directly impacts sensor placement, imaging angle, and leak quantification accuracy in real-world detection systems.

Similarly, adjusting the leak inlet velocity, which directly contributes to the leak rate (as in equation 2.15) affects the initial momentum of the release. As shown in Figure 5.8, high-velocity leaks (e.g. 50-100 m/s) generate narrow, fast-rising jets that maintain a focused structure over longer distances. In contrast, lower inlet velocities (e.g., 1-5 m/s) result in broader, more diffuse plumes that are quickly dominated by wind advection. This trend highlights how leak rate governs the transition between momentum-driven and wind-dominated dispersion regimes.

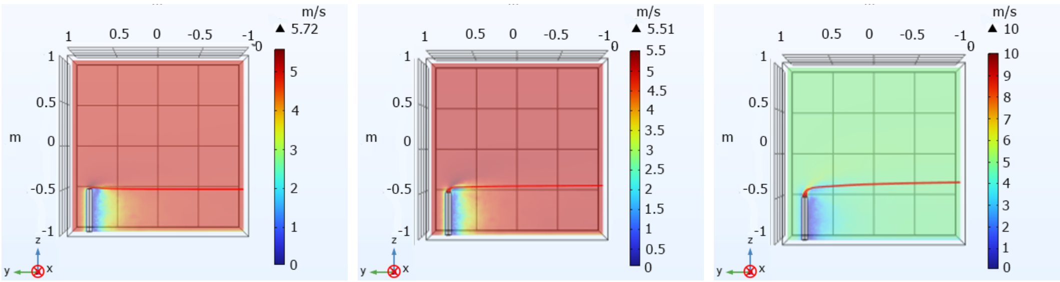

(a) Inlet velocity 1 m/s (b) Inlet velocity 5 m/s (c) Inlet velocity 10 m/s

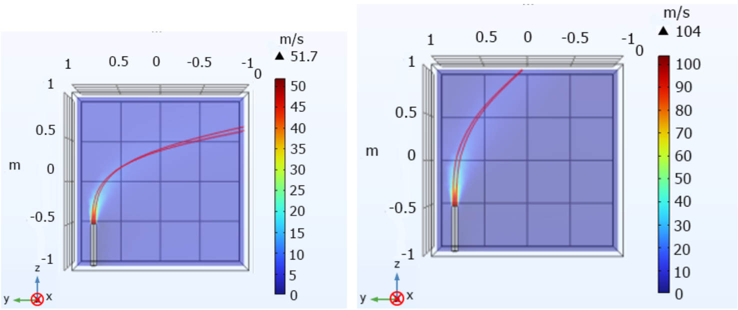

(d) Inlet velocity 50 m/s (e) Inlet velocity 100 m/s

Figure 5.8: Side-view velocity magnitude slices with streamlines for various leak inlet velocities under constant wind speed (5 m/s).

Projection Views

To prepare the volumetric CFD simulation data for image-based leak rate quantification, the 3D concentration fields are projected onto 2D planes by integrating along lines of sight, as discussed in Section 4.3. This operation recreates how a remote gas-sensing system would perceive the plume from various observational viewpoints.

For each simulation case, three canonical 2D projections were generated corresponding to top (x–y), side (y–z), and front (x–z) views, as illustrated in Figure 5.9. These projections preserve key spatial concentration features and offer a realistic representation of how the plume appears from various perspectives. Each view simulates a virtual observation along its orthogonal axis (z, x, and y, respectively).

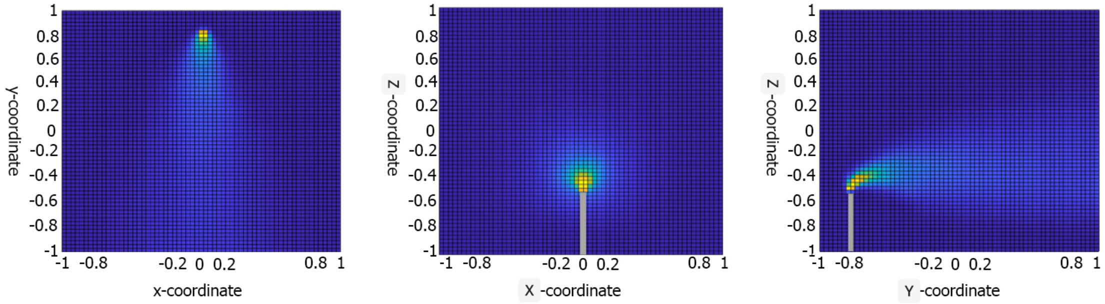

Figure 5.9: Path Integrated concentrations of the methane plume in 3 standard views, simulating sensor views for remote sensing analysis.

As mentioned in Section 4.4, only projections that align with the wind direction (y axis) are informative for leak-rate quantification. In the present geometry, those are the XY and YZ planes. Either of these views is, in principle, sufficient for the leak rate quantification algorithm introduced in section 4.4, however, the second is retained for cross-checking.

5.3 Image-Based Leak Rate Estimation

To support the image-based quantification method, a series of CFD simulations was conducted to generate a controlled dataset. These simulations span a range of leak rates, wind velocities, and leak source sizes, designed to reflect diverse but realistic field scenarios.

The corresponding 2D projections capture a diverse set of plume shapes and concentrations, providing a rigorous basis for evaluating the quantification algorithm. As shown in Figure 5.10, the selected cases correspond to leak rates of approximately 100, 1000, and 10,000 g/h, and the projections are taken in the YZ plane, one of the most informative view for quantification (refer to Section 4.4.

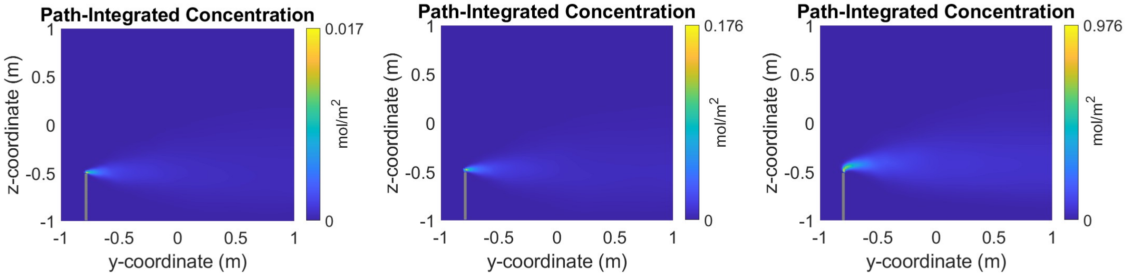

(a) ∼100 g/h emission rate (b) ∼1000 g/h emission rate (c) ∼10,000 g/h emission rate

Figure 5.10: Path-integrated methane concentration projections (YZ plane) at varying emission rates.

To ensure meaningful comparisons across cases, the leak radius was adjusted to modify the total mass flow rate while keeping the exit velocity constant, thus preserving realistic flow structure without requiring computational domain expansion. Each case uses a fixed cubic domain of 2 m × 2 m × 2 m, and the images were rendered at resolutions of 64 (or higher number of) pixels depending on the size of the plume.

The mass flow rates, $\dot{m}$, were estimated with quantification basis introduced in Section 4.4 based on path-integrated methane gas concentrations.

5.4 Mesh Resolution Sensitivity Analysis

In this section, a mesh refinement analysis is performed, and the model's sensitivity to mesh resolution is discussed in relation to the accuracy and reliability of image-based methane mass flow rate quantification. In CFD, mesh resolution significantly affects the ability to resolve steep gradients near the leak source and throughout the plume, particularly in early mixing regions. Coarse grids tend to introduce numerical diffusion and under-resolve the plume features, which can degrade the accuracy of path-integrated concentration and result in error in leak rate estimates.

Four mesh configurations (M-0 to M-3) are evaluated, each with progressively finer resolution, as summarized in Table 5.1. The coarsest grid, M-0 ($\sim$ 139,000 elements), is used only for preliminary testing and was not employed for quantitative evaluation. The baseline mesh, M-1, with approximately 720,000 elements served as the default configuration for most simulations. A more refined mesh, **M-2**, increased resolution near the leak source using local refinement and boundary layers, totaling $\sim$ 1.3 million elements.

Further refinement to **M-3** ($\sim$ 4.3 million elements) applied more aggressive corner and global refinement, but produced negligible change in plume shape and quantification error estimate. This confirms that mesh independence was achieved and that M-2 provides sufficient resolution for accurate quantification without having excessive computational cost.

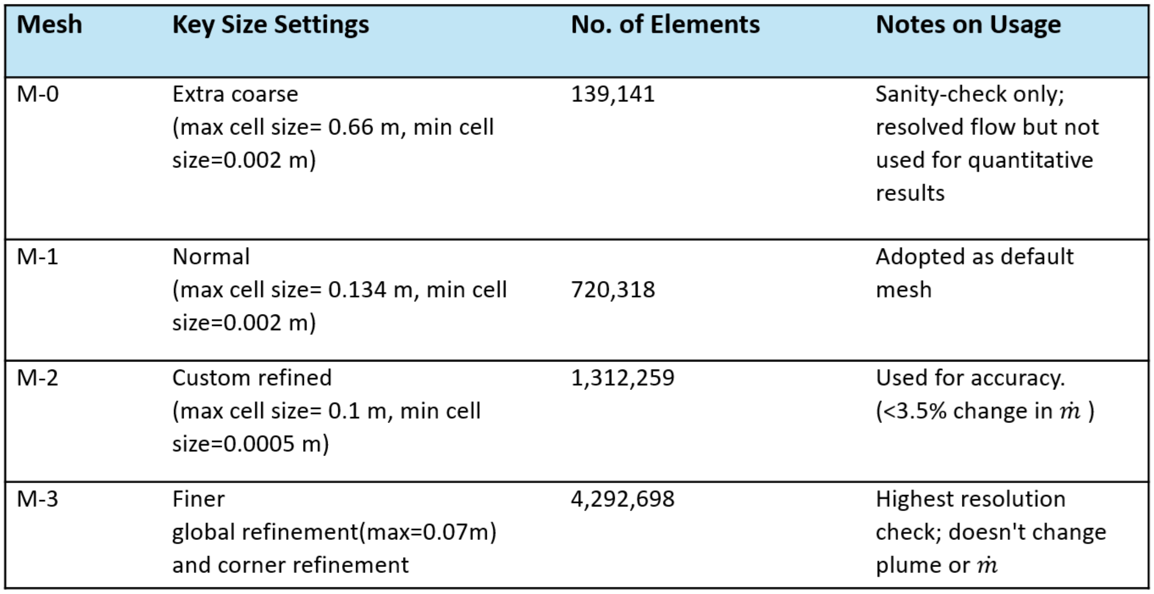

Mesh	Key Size Settings	No. of Elements	Notes on Usage
M-0	Extra coarse (max cell size= 0.66 m, min cell size=0.002 m)	139,141	Sanity-check only; resolved flow but not used for quantitative results
M-1	Normal (max cell size= 0.134 m, min cell size=0.002 m)	720,318	Adopted as default mesh
M-2	Custom refined (max cell size= 0.1 m, min cell size=0.0005 m)	1,312,259	Used for accuracy. (<3.5% change in $\dot{m}$)
M-3	Finer global refinement(max=0.07m) and corner refinement	4,292,698	Highest resolution check; doesn't change plume or $\dot{m}$

Table 5.1: Summary of mesh configurations used in the mesh sensitivity study.

Figure 5.11 illustrates the impact of mesh resolution on the accuracy of image-based leak quantification. The plot compares the relative error (%) in the estimated leak rate as a function of downstream distance from the leak source, for two mesh configurations: M-1 (baseline) and M-2 (refined). These results correspond to a known leak rate of 0.36 kg/h under a 5 m/s wind condition.

Closer to the leak (within 0.2 m), the coarser mesh (M-1) exhibits up to 10% relative error, whereas M-2 maintains nearly 0–2% error, attributed to its finer resolution near the source, which is expected behavior in CFD. This highlights how coarse meshes may under-resolve concentration gradients in the near field, which leads to early integration inaccuracies.

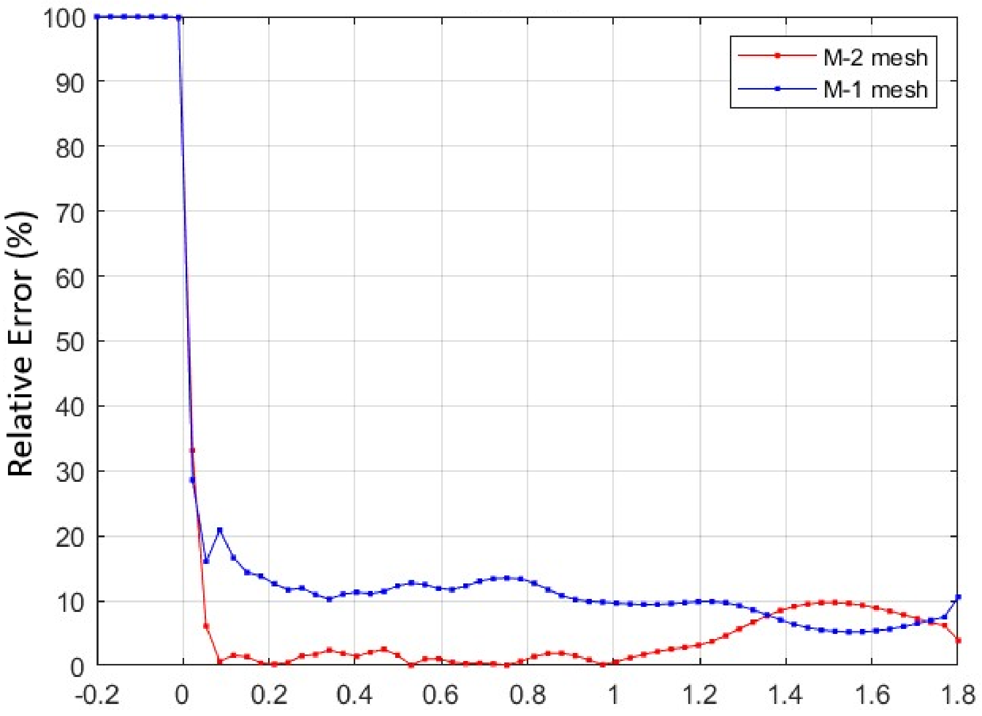

Figure 5.11: Mesh sensitivity analysis: relative error (%) in estimated mass flow rate versus downstream distance.

While the error curves from both meshes tend to converge beyond 1 m downstream, M-2 consistently exhibits a flatter and lower error profile, confirming that its refinements improve both numerical fidelity and early plume resolution.

Based on mesh sensitivity analysis, M-2 was selected as the final mesh for quantification studies. It offers a good balance between numerical accuracy and computational efficiency. The negligible difference between M-2 and the high-resolution M-3 case further validates mesh convergence. Overall, this mesh sensitivity analysis supports the numerical robustness of the proposed image-based quantification method and confirms that, when properly designed, the mesh will not bias the results.

5.5 Quantitative Analysis

To evaluate the accuracy of image-based quantification approach, the estimated mass flow rate was compared against the true CFD injection (or computed) rate for several leak scenarios. Table 5.2 demonstrates the comparing leak rate results corresponding to the three cases shown in Figure 5.10. It summarizes the numerical accuracy of the image-based estimated leak rates versus CFD truth.

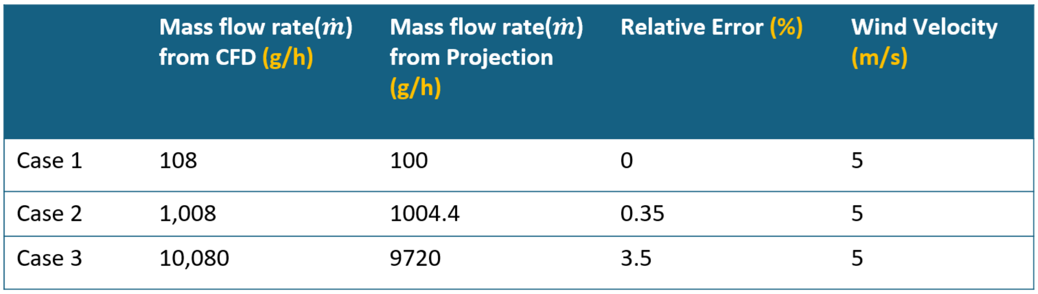

	Mass flow rate($\dot{m}$) from CFD (g/h)	Mass flow rate($\dot{m}$) from Projection (g/h)	Relative Error (%)	Wind Velocity (m/s)
Case 1	108	100	0	5
Case 2	1,008	1004.4	0.35	5
Case 3	10,080	9720	3.5	5

Table 5.2: Comparison of mass flow rate estimates from image-based projection and CFD ground truth across three leak scenarios.

Despite increasing plume complexity at higher leak rates (up to 10,000 g/h), the quantification algorithm maintains strong performance, with relative errors below 4%. These results validate the feasibility of inferring methane emission rates from projected data under controlled conditions and support the utility of image-based techniques for field-deployable monitoring systems.

Table 5.3 presents the estimated leak rates from the projection method compared with the CFD reference values, along with the corresponding relative errors for cases with different wind velocities. The results show that the relative error increases as wind speed decreases. At lower wind velocities, the method becomes more challenging to apply because capturing the plume's steady-state behavior in the downwind direction would require a substantially larger computational domain. Such an extension is not numerically feasible within the scope of this study. Consequently, the higher errors at lower wind speeds are attributed to the incomplete development of the plume within the simulated domain.

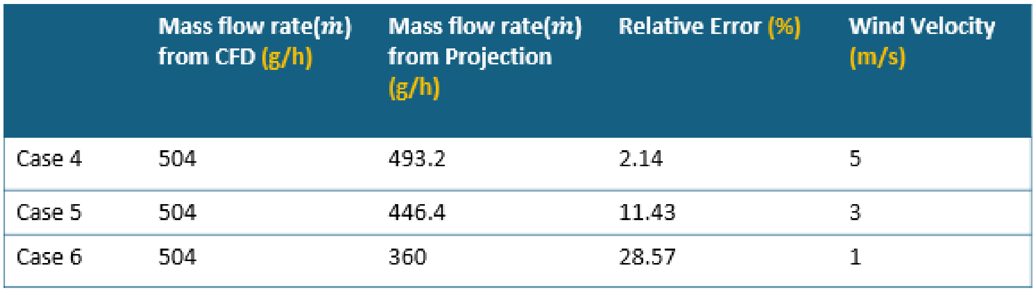

	Mass flow rate($\dot{m}$) from CFD (g/h)	Mass flow rate($\dot{m}$) from Projection (g/h)	Relative Error (%)	Wind Velocity (m/s)
Case 4	504	493.2	2.14	5
Case 5	504	446.4	11.43	3
Case 6	504	360	28.57	1

Table 5.3: Comparison of mass flow rate estimates from image-based projection and CFD ground truth across three wind conditions.

5.6 Optimal Imaging Distance for Quantification

Accurate leak rate estimation from projected concentration data requires selecting an appropriate downstream observation distance. As defined in the image-based quantification method introduced earlier, performing the integration too close to the leak source leads to unreliable results. In this region, the plume is still forming, mixing is incomplete, and sharp gradients can introduce numerical instability. Conversely, observations taken sufficiently far downstream allow the plume to stabilize and fully develop, conditions under which line-of-sight integration yields robust and consistent mass flow estimates.

To identify such a region for this study, a parametric sweep was conducted in MATLAB across a set of virtual planes positioned at increasing distances downstream of the leak source. For each plane, the methane mass flow rate was computed using the projected concentration field and wind velocity. The analysis shown in Figures 5.12 and 5.13, are performed for a representative case with a leak rate of 2.8×10^{-5} kg/s (e.g. ~100 g/h) and a wind speed of 5 m/s.

Figure 5.12 shows the estimated mass flow rate ($\dot{m}$) versus distance from the leak origin. At very short distances from the source, the estimated values deviate significantly from the known CFD mass flow rate (e.g. 2.8×10^-5 kg/s). Beyond 0.8-1 meter from the leak source downstream, the curve flattens and approaches the true value, indicating that the plume has stabilized.

Figure 5.13 presents the relative error (%) between the image-based estimate and the CFD reference of $\dot{m}$. Close to the leak source, the error is high due to transient effects and unresolved gradients but falls below 3% beyond ~ 0.8 m.

To formally define this optimum quantifaction distance, two criteria were considered: A relative error threshold of 3% for accuracy, and a slope threshold of 1% indicating stabilization.

Based on these criteria, 0.816 m downstream was identified as the optimal location for this case shown in Figures 5.13 and 5.12.

The optimum distance represents a point where the plume is sufficiently developed and early mixing transients no longer affect the results. This optimum distance is not universal and is expected to vary with different leak rates and wind conditions. Higher leak velocities or buoyancy-dominated plumes may require longer distances for stabilization, whereas stronger wind fields help accelerate plume development and reduce the required observation length.

In practice, defining a quantification threshold based on stability and error control provides a rational basis for sensor placement and ensures that quantification avoids early-region inaccuracies or inefficient computations. In the context of this thesis, this analysis supports the reliability of the image-based quantification method and serves as a practical guide for choosing observation distances in both simulation and real-world scenarios.

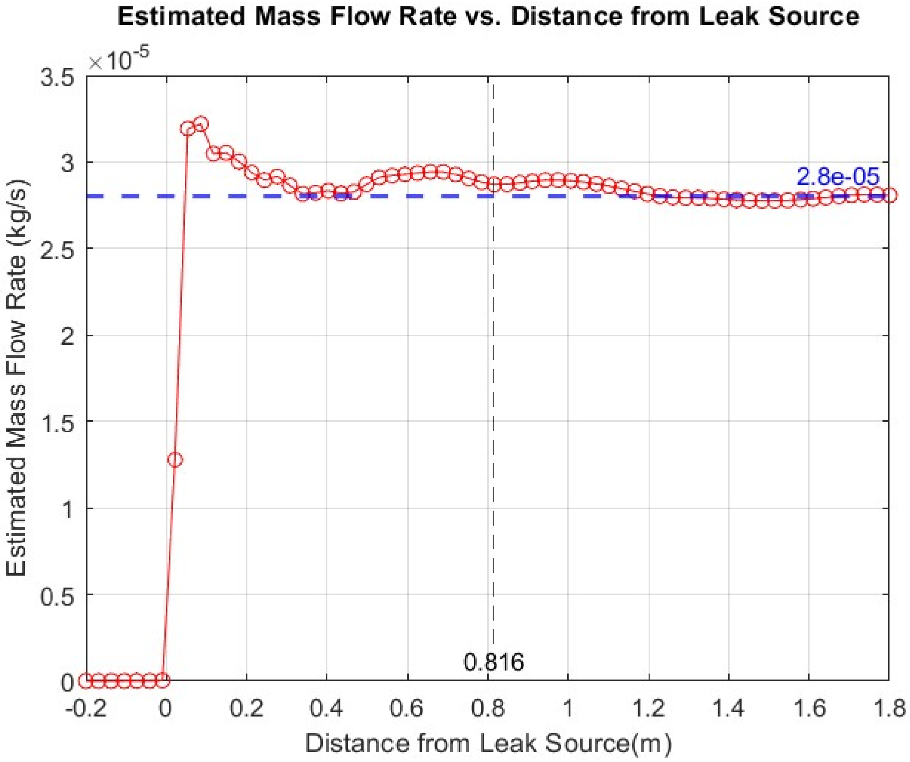

Figure 5.12: Estimated mass flow rate versus downstream distance from the leak source. The true CFD $\dot{m}$ value is shown as a dashed line. 2.8e-5 kg/s corresponds to 100 g/h leak rate

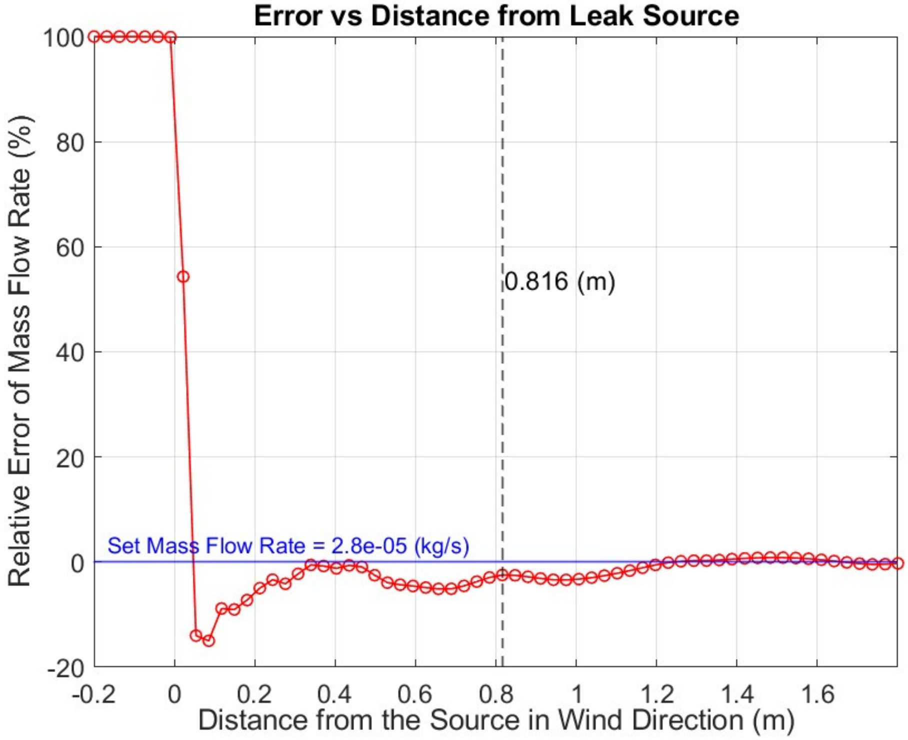

Figure 5.13: Relative error in image-based mass flow estimation versus downstream distance. Optimum distance is identified where error and slope thresholds are satisfied.

Chapter 6

Conclusion and Future Work

6.1 Conclusion

This thesis addressed the challenge of methane leak rate quantification through a hybrid approach that combines CFD-based plume simulations with 2D projection techniques, in order to generate synthetic image datasets suitable for integration-based analysis. The method draws inspiration from remote optical gas sensing systems and is grounded in the Beer–Lambert law and the principle of mass conservation. The central aim was to evaluate whether realistic leak scenarios can be reliably quantified using image-derived data and, importantly, to determine under what physical and computational conditions the method remains accurate.

A full 3D simulation framework was developed using COMSOL Multiphysics to model methane releases into ambient wind, accounting for both transient jet behavior and steady-state dispersion. These simulations were first validated against a literature-reported case, covering different leak lates and wind velocities. The main findings confirmed that plume evolution stabilizes rapidly under moderate wind speeds, often within a few tenths of a second, and within a meter from the source, indicating that short-range, real-time quantification is physically feasible.

To connect CFD outputs with image-based diagnostics, the volumetric concentration fields were projected onto 2D planes (XY, YZ, and XZ), simulating the line-of-sight measurement used by optical sensing systems. These projections were processed by a custom MATLAB-based algorithm that estimates methane mass flow rate ($\dot{m}$) through a simple but effective integration of path-integrated concentration and velocity across the selected quantification plane.

This quantification method was applied across a range of wind speeds, leak rates, and source geometries. Across all cases studied, the image-based approach demonstrated relative errors below 4%, even when plume shape and transport dynamics varied. An analysis of quantification performance across different downstream locations led to the identification of an optimum distance, which varied, depending on leak and environmental conditions. At this point, the plume was sufficiently developed and mixing effects had stabilized, improving accuracy and robustness. Additionally, a mesh sensitivity analysis showed that further grid refinement beyond the M-2 configuration (~ 1.3 million elements) did not significantly alter results, confirming mesh independence and reinforcing the method's computational stability.

Importantly, this study demonstrated that accurate methane mass flow estimation is possible without any explicit knowledge of local velocity, leak source geometry, or leak cross-sectional area; only with path-integrated concentration fields and background wind speed can result in accurate estimation of leak flow rate. This capability opens up several practical applications in sensor calibration, simulation-assisted training, and rapid assessment during field deployments where estimating leak severity is critical for timely mitigation.

6.2 Observations and Limitations

While the results presented in this study are promising, several limitations must be acknowledged.

First, the method assumes uniform wind profiles and non-turbulent atmospheric conditions, which simplifies the external environment compared to real-world field scenarios. In reality, topography, structures, and stochastic wind variations can introduce complex dispersion behaviors that may affect quantification.

Second, the projection-based quantification assumes a fully developed plume across the quantification plane, which is a key assumption in ensuring valid mass flow calculations. While this was verified in the current study via CFD outputs and error analysis, this condition may not hold in shorter domains or in the presence of obstacles and terrain-induced distortions. The use of optimum distance downstream helps mitigate this, but must be tailored to each case.

Third, no sensor noise or image degradation effects were included in the projected images since the dataset include only simulation outputs. Real camera or spectroscopy systems are subject to optical limitations, calibration drift, and signal-to-noise constraints that were not modeled here. Consequently, the performance metrics shown represent an idealized upper bound on accuracy.

Despite these simplifications, the approach developed here offers a solid and well-validated foundation for extending image-based quantification techniques to more realistic and practical methane sensing systems.

6.3 Future Work

Building on the outcomes of this thesis, several research directions can be pursued to enhance and generalize the proposed framework.

One important extension is to incorporate sensor realism by modeling camera optics, beam divergence, detector noise, and off-axis viewing effects. This would provide a more representative analysis of how measurement uncertainties propagate into $\dot{m}$ estimation and would bring the framework closer to practical deployment.

Another area for development is the inclusion of atmospheric turbulence and unsteady wind fields. Future CFD simulations could utilize more rigorous turbulent models that account for eddies or stochastic wind boundary conditions to capture the influence of turbulence on plume shape, dispersion, and quantification stability.

The quantification plane selection could also be automated or adapted dynamically in response to plume behavior. For real-time field applications, it may be necessary to implement algorithms that detect where the plume becomes stable and adapt the integration plane accordingly.

A critical next step is field validation. While CFD served as ground truth in this thesis, applying the method to controlled release experiments (e.g., in wind tunnels or instrumented test sites) would strengthen its credibility and practical relevance. Bridging this gap between simulation and real-world measurement is a key to transitioning the framework into operational settings.

Additionally, expanding the method to include multiple concurrent leaks would allow the approach to be tested under complex flow interactions. Field settings may include multiple leak sources, a factor that could challenge the assumptions made here.

The method could also be also generalizable across different greenhouse gas species. Provided concentration maps are available, the same framework could be applied to estimate emissions of CO_2, extending its use into broader environmental monitoring.

Finally, integration into full leak detection systems would be a promising application of this methodology. By combining detection and quantification modules, a complete real-time methane monitoring solution could be developed.

6.4 Summary

In summary, this thesis presented a novel, simulation-informed, image-based quantification framework for methane leak assessment. The method was shown to be both physically grounded and numerically robust, capable of achieving low error rates across a broad range of controlled leak conditions. While it relies on idealized assumptions at this stage, the foundation laid here can support future research, tool development, and operational sensing in the context of methane mitigation and environmental monitoring.

With increasing regulatory and societal attention on methane as a potent greenhouse gas, tools that enable rapid, remote, and accurate quantification are urgently needed. The work here makes a concrete step in this direction.

Bibliography

[1] IPCC. Climate change 2021: The physical science basis. contribution of working group i to the sixth assessment report of the intergovernmental panel on climate change, 2021. Accessed: 2025-07-06.

[2] K. A. Mar, C. Unger, L. Walderdorff, and T. Butler. Beyond co2 equivalence: The impacts of methane on climate, ecosystems, and health. *Environmental Science Policy*, 134:127–136, 2022.

[3] U.S. Environmental Protection Agency. Inventory of U.S. greenhouse gas emissions and sinks: 1990–2022. Technical Report EPA 430-R-24-004, U.S. Environmental Protection Agency, Washington, DC, 2024. Accessed 6 July 2025.

[4] Environment and Climate Change Canada. Review of canada's methane regulations for the upstream oil and gas sector. Technical report, Environment and Climate Change Canada, 2021. Executive Summary—"Methane makes up about 13

[5] K. MacKay, M. Lavoie, E. Bourlon, E. Atherton, E. O'Connell, J. Baillie, C. Fougère, and D. Risk. Methane emissions from upstream oil and gas production in canada are underestimated. *Scientific Reports*, 11(1):8041, April 2021.

[6] E. Chan, D. E. J. Worthy, D. Chan, M. Ishizawa, M. D. Moran, A. Delcloo, and F. Vogel. Eight-year estimates of methane emissions from oil and gas operations in western canada are nearly twice those reported in inventories. *Environmental Science & Technology*, 54(23):14899–14909, 2020.

[7] Global Methane Pledge. Global methane pledge: A voluntary agreement to reduce anthropogenic methane emissions by at least 30% from 2020 levels by 2030. https://www.globalmethanepledge.org/, 2021. Launched at COP26; accessed July 6, 2025.

[8] W. J. Sawyer, I. Genina, R. J. Brenneis, H. Feng, Y. Li, and S.-X. L. Luo. Methane emissions and global warming: Mitigation technologies, policy ambitions, and global efforts. *MIT Science Policy Review*, 3, aug 29 2022. https://sciencepolicyreview.pubpub.org/pub/ea652for.

[9] A. P. Ravikumar, D. Roda-Stuart, R. Liu, A. Bradley, J. Bergerson, Y. Nie, S. Zhang, X. Bi, and A. R. Brandt. Repeated leak detection and repair surveys reduce methane emissions over scale of years. *Environmental Research Letters*, 15(3):034029, feb 2020.

[10] D. J. Jacob, D. J. Varon, D. H. Cusworth, P. E. Dennison, C. Frankenberg, R. Gautam, L. Guanter, J. Kelley, J. McKeever, L. E. Ott, B. Poulter, Z. Qu, A. K. Thorpe, J. R. Worden, and R. M. Duren. Quantifying methane emissions from the global scale down to point sources using satellite observations of atmospheric methane. *Atmospheric Chemistry and Physics*, 22(14), 2022.

[11] U.S. Environmental Protection Agency. Epa issues final requirements for using optical gas imaging in leak detection. Technical report, U.S. Environmental Protection Agency, 2023. Accessed July 6, 2025. Expresses methane leak rates in grams per hour (g/h).

[12] R. Kouznetsov, R. Hänninen, A. Uppstu, E. Kadantsev, Y. Fatahi, M. Prank, D. Kouznetsov, S. M. Noe, H. Junninen, and M. Sofiev. A bottom-up emission estimate for the 2022 nord stream gas leak: derivation, simulations, and evaluation. *Atmospheric Chemistry and Physics*, 24(8):4675–4691, 2024.

[13] T. E. Darcie, R. L. Smith, and N. N. Tzonev. System and method for remote imaging of greenhouse gas emissions, May 1 2025. US Patent App. 18/837,060.

[14] J. Wang, J. Ji, A. P. Ravikumar, S. Savarese, and A. R. Brandt. Videogasnet: Deep learning for natural gas methane leak classification using an infrared camera. *Energy*, 238:121516, 2022.

[15] D. Cusworth, R. Duren, A. Thorpe, W. Olson-Duvall, J. Heckler, J. Chapman, M. Eastwood, M. Helmlinger, R. Green, G. Asner, P. Dennison, and C. Miller. Intermittency of large methane emitters in the permian basin. *Environmental Science Technology Letters*, 06 2021.

[16] A. P. Ravikumar, S. Sreedhara, J. Wang, J. Englander, D. Roda-Stuart, C. Bell, D. Zimmerle, D. Lyon, I. Mogstad, B. Ratner, and A. R. Brandt. Single-blind inter-comparison of methane detection technologies – results from the stanford/edf mobile monitoring challenge. *Elementa: Science of the Anthropocene*, 7:37, 09 2019.

[17] A. P. Ravikumar, J. Wang, and A. R. Brandt. Are optical gas imaging technologies effective for methane leak detection? *Environmental Science & Technology*, 51(1):718–724, 2017. PMID: 27936621.

[18] P. Werle, F. Slemr, K. Maurer, R. Kormann, R. Mücke, and B. Jänker. Near- and mid-infrared laser-optical sensors for gas analysis. *Optics and Lasers in Engineering*, 37(2):101–114, 2002. Optical Methods in Earth Sciences.

[19] G. Stewart. *Laser and Fiber Optic Gas Absorption Spectroscopy.* Cambridge University Press, Cambridge, 2021.

[20] S. Lin, J. Chang, J. Sun, and P. Xu. Improvement of the detection sensitivity for tunable diode laser absorption spectroscopy: A review. *Frontiers in Physics*, Volume 10 - 2022, 2022.

[21] A. S. Ashik, P. J. Rodrigo, H. E. Larsen, N. T. Vechi, K. Kissas, A. M. Fredenslund, J. G. Mønster, C. Scheutz, and C. Pedersen. Integrated-path multi-gas sensor using near-infrared diode lasers: An alternative to vehicle-driven point gas analyzer. *Sensors and Actuators B: Chemical*, 412:135855, 2024.

[22] C. S. Goldenstein, R. M. Spearrin, J. B. Jeffries, and R. K. Hanson. Infrared laser-absorption sensing for combustion gases. *Progress in Energy and Combustion Science*, 60:132–176, 2017.

[23] C. S. Goldenstein, R. M. Spearrin, J. B. Jeffries, and R. K. Hanson. Infrared laser-absorption sensing for combustion gases. *Progress in Energy and Combustion Science*, 60:132–176, 2017.

[24] Zurich Instruments. Principles of lock-in detection, 2016. Accessed: 2025-07-23.

[25] S. Cwalina, C. Kottke, V. Jungnickel, R. Freund, P. Runge, P. Rustige, T. Knieling, S. Gu-Stoppel, J. Albers, N. Laske, F. Senger, L. Wen, F. Giovanneschi, E. Altuntac, A. N. Ramesh, M. A. González-Huici, A. Küter, and S. Reddy.

Fiber-based frequency modulated lidar with mems scanning capability for long-range sensing in automotive applications. In *2021 IEEE International Workshop on Metrology for Automotive (MetroAutomotive)*, pages 48–53, 2021.

[26] X. Lou, Y. Feng, C. Chen, and Y. Dong. Multi-point spectroscopic gas sensing based on coherent fmcw interferometry. *Optics Express*, 28:9014–9026, 03 2020.

[27] G. P. Agrawal. *Fiber-Optic Communication Systems*. John Wiley & Sons, New York, 4th edition, 2010.

[28] P. J. P. Lindelöw. *Fiber Based Coherent Lidars for Remote Wind Sensing*. PhD thesis, Technical University of Denmark (DTU), Lyngby, Denmark, March 2008.

[29] Y. Zeng and J. Morris. Detection limits of optical gas imagers as a function of temperature differential and distance. *Journal of the Air & Waste Management Association*, 69(3):351–361, 2019.

[30] E. Özsoy. *Geophysical Fluid Dynamics I: An Introduction to Atmosphere–Ocean Dynamics: Homogeneous Fluids*. Springer Textbooks in Earth Sciences, Geography and Environment. Springer, 2020.

[31] M. T. Schobeiri. *Fluid Mechanics for Engineers: A Graduate Textbook*. Springer-Verlag Berlin Heidelberg, 2010.

[32] P. J. Pritchard. *Fox and McDonald's Introduction to Fluid Mechanics, 8th Edition*. John Wiley & Sons, 2010.

[33] B. R. Munson, T. H. Okiishi, W. W. Huebsch, and A. P. Rothmayer. *Fundamentals of Fluid Mechanics*. Wiley, 2013.

[34] B. J. Cantwell. *Fundamentals of Compressible Flow*. Stanford University, Department of Aeronautics and Astronautics, Stanford, CA, 2022.

[35] R. Edie, A. M. Robertson, R. A. Field, J. Soltis, D. A. Snare, D. Zimmerle, C. Bell, T. L. Vaughn, and S. M. Murphy. Constraining the accuracy of flux estimates using otm 33a. *Atmospheric Measurement Techniques*, 13:341–353, January 2020.

[36] H. Wilkening and D. Baraldi. Cfd modelling of accidental hydrogen release from pipelines. *International Journal of Hydrogen Energy*, 32(13):2206–2215, 2007. ICHS-2005.